Genetically- and spatially-defined basolateral amygdala neurons control food consumption and social interaction

Hansol Lim[1], Yue Zhang[2], Christian Peters[1], Tobias Straub[3], Johanna Luise Mayer [1], Rüdiger Klein[1*]

1. Department Molecules – Signaling – Development, Max Planck Institute for Biological Intelligence, Martinsried, Germany

2. Department Synapses – Circuits - Plasticity, Max Planck Institute for Biological Intelligence, Martinsried, Germany

3. Biomedical Center Core Facility Bioinformatics, LMU, Munich, Germany

*Correspondence: ruediger.klein@bi.mpg.de (R.K.)

Highlights:

1) Classification of molecularly-defined glutamatergic neuron types in mouse BLA with distinct spatial expression patterns.
2) BLA^{Lypd1} neurons are positive-valence neurons innately responding to food and promoting normal feeding.
3) BLA^{Etv1} neurons innately represent aversive and social stimuli.
4) BLA^{Etv1} neurons promote fear learning and social interactions.

Abstract

The basolateral amygdala (BLA) contains discrete neuronal circuits that integrate positive or negative emotional information and drive the appropriate innate and learned behaviors. Whether these circuits consist of genetically-identifiable and anatomically segregated neuron types, is poorly understood. Also, our understanding of the response patterns and behavioral spectra of genetically-identifiable BLA neurons is limited. Here, we classified 11 glutamatergic BLA cell clusters and found that several of them were anatomically segregated in lateral versus basal amygdala, and anterior versus posterior regions of the BLA. Two of these BLA subpopulations innately responded to valence-specific, whereas one responded to mixed - aversive and social - cues. Positive-valence BLA neurons promoted normal feeding, while mixed selectivity neurons promoted fear learning and social interactions. These findings enhance our understanding of cell type diversity and spatial organization of the BLA and the role of distinct BLA populations in representing valence-specific and mixed stimuli.

Introduction

The basolateral complex of the amygdala (BLA) processes and encodes the emotional valence of salient cues and controls the appropriate behavioral output. Current models posit that aversive and rewarding stimuli may involve discrete neural circuits to elicit responses ranging from defensive to appetitive behaviors [1,2]. The distinction of these neural circuits is, however, incompletely understood and many questions remain unanswered: Are the BLA neurons that encode positive or negative values genetically distinct and do they occupy discrete spatial locations within the BLA? Do individual BLA neurons innately represent one type of stimuli, or can they represent mixed selectivity? Currently, there is evidence for all of these scenarios. Genetically distinct BLA neurons controlling valence-specific motivated behavior have been previously described [3,4]. Conversely, distinct appetitive and aversive networks in BLA were described based on their segregated projections to nucleus accumbens (Nac) and central amygdala (CeA) [5,6]. Such output specificity may be determined during development by genetically-encoded guidance cues, but this remains to be demonstrated [7]. Single cell recordings have shown that genetically-defined BLA neurons are typically quite heterogeneous with fractions of cells responding to positive and negative cues [4,8,9]. To what extent these variable responses to multiple stimuli reflect the cell type or the result of changes in internal state of the animals, including anxiety, arousal, sensory processing, or previous experience remains to be determined [10–12].

One experimental approach that could provide insights into this diversity of BLA response is single cell transcriptomics (scRNAseq) which enables the identification of cell types on the basis of similar gene-expression properties [13]. Coupling transcriptomic cell typing with their spatial organization, input-output pathways, and functional analyses has the potential to reveal the organizational framework of the BLA. A previous scRNAseq analysis of excitatory neurons of the BLA has revealed two main principles: First, the anatomical division of the BLA into lateral (LA)

and basal amygdala (BA) was recapitulated in a discrete separation of transcriptomic cell types arguing that excitatory neurons of the LA and BA should be considered distinct [14]. Second, within LA and BA, the analysis revealed anterior-posterior continuous gene-expression differences instead of discrete cell types. However, this organization was inconsistent with previous anatomical parcellations of the BLA [15–17] and no functional analysis was included in the O'Leary study, we performed our own single cell transcriptomic and spatial analysis of BLA neurons.

A complementary approach to map BLA circuit organization is to functionally characterize genetically-defined small subpopulations of BLA neurons and to expand the repertoire of valence-specific behavioral tests. Previous behavioral studies were inspired by BLA lesions which caused profound behavioral disturbances, typically focusing on motivated behavior, including aversive [18,19], appetitive [20–22], and instrumental conditioning paradigms [23–26], as well as addictive [27,28] and anxiety behaviors [29–32].

Somewhat surprisingly, the BLA has not been implicated in the normal consumption of food. Rather, published work indicates that BLA principle neurons (PN) promote reward (sucrose) consumption in an instrumental goal-directed action performance test [33], and that BLA-Nac projections enhanced instrumental food consumption in a chronic stress paradigm, but not free-feeding behavior [34]. Moreover, BLA activity decreased the likelihood of food consumption in a risky environment [35], suggesting that the BLA regulates risk behavior when animals forage for food. Since BLA neurons were recently shown to increase firing in response to food [8,36], we here asked whether the manipulation of distinct BLA PN populations may reveal contributions to the control of normal feeding.

The BLA has also been implicated in social behavior in humans and rodents [30,37,38]. Social behavior is complex and can be rewarding, but also upsetting. It activates the brain's reward circuitry [39], but can also trigger avoidance and aggression [40–42]. Hence, social interactions can have positive and negative valence [43]. Optogenetic inactivation of the BLA facilitates social

interactions [44], suggesting that the BLA specifically mediates aversive aspects of social interaction. Consistent with such a conclusion, the same BLA projection to ventral hippocampus (vHPC) mediates social and anxiety-related behaviors [45]. More recently, it was shown that the BLA encodes social exploration behavior in a valence-independent manner by two functionally anticorrelated ensembles, consistent with multiplexed representation of valence in the BLA [46]. Whether or not the BLA contains genetically-defined PN subpopulations that can regulate social interactions is unknown.

Here, we provide a full description of the genetic diversity of glutamatergic BLA neurons and their spatial distribution. We characterized a total of 11 cell clusters and demonstrated that they distributed in distinct spatial BLA subregions. Unsupervised approaches using dimensionality reduction and cross-correlation of meta datasets suggest that distinct cell clusters are present within LA and BA subregions. We selected three genetically-defined neuron populations each representing two or three transcriptional clusters, for subsequent functional analysis. We characterized a positive-valence subpopulation that increased activity in response to the presence of food and promoted innate feeding. A second population showed mixed selectivity by responding to aversive and social cues, and not only promoted defensive, but also social behavior. A third population followed the classical BLA model of an aversive population by not responding to food and social cues and promoting aversive conditioning. These findings enhance our understanding of cell type diversity and spatial organization of the BLA and the role of distinct BLA PN populations in innate food consumption and social behavior.

Results

Single-nuclei RNAseq identifies molecularly-defined glutamatergic BLA cell types

We characterized transcriptomic cell types using single-nuclei RNA sequencing (snRNAseq) from the adult BLA, spanning 2.4 mm in anterior-posterior direction (Fig. 1A). To spatially annotate the

cell clusters, we used a regional parcellation method as published previously[17] (Fig. 1B). Our initial analysis of the BLA transcriptomic dataset identified seven transcriptomic cell types, including 3,278 non-neuronal and 4,544 neuronal cells (Extended Data Fig. 1A, B). We re-clustered the neuronal cells only and separated them into GABAergic and glutamatergic neurons using specific markers for inhibitory (*Gad1, Gad2* and *Slc32a1*) and excitatory neurons (*Slc17a7*) (Fig. 1C). Separate re-clustering of GABAergic neurons revealed 10 clusters, including intercalated cells (ITC) and amygdalostriatal area cells (marked by *Foxp2* and *Rarb*, respectively) and a newly identified cluster marked by *Tshz2* and *Rmst* which appeared to be equally related to ITC and BLA GABAergic interneurons (Extended Data Fig. 1C, D). The latter neurons were separated into two populations marked by *Reln* and *Calb1* (Extended Data Fig. 1D). The *Calb1* population included *Calb1, Sst* and *Htr2a* clusters, while the *Reln* population contained *Lamp5, Ndnf,* and *Cck* clusters (Extended Data Fig. 1D), showing distinct transcriptomes and correlations with each other (Extended Data Fig. 1E). These findings agreed well with recent scRNA-seq studies from cortex and BLA [47–49].

Separate re-clustering of glutamatergic BLA cells identified 12 clusters including one cluster (cluster 10) from posterior medial amygdala (MEAp) marked by *Esr1* and *Pde11a* 5 (Fig. 1D, E). Compared to GABAergic clusters, glutamatergic clusters shared many of their top 5 marker genes. For example, all top 5 genes for cluster 2 (cl2) were also expressed in cl6. *Rspo2* was expressed in cl1 and 11, and *Rorb* in cl7 and cl8 (Fig. 1D). To identify distinctive marker combinations for glutamatergic clusters, we first calculated the top marker genes for each cluster using an AUC (area under the curve) threshold of 0.5 and a minimum observation percentage of 20 (see methods). We then chose genes expressed exclusively in one or two clusters. Through this analysis, we identified a minimum of three representative genes for each cluster (Fig. 1F). We then inspected the spatial expression of each marker in the Allen brain atlas and selected 10 genes that appeared to be expressed in subregions of the BLA (Extended Data Fig. 1F). Marker

genes that were expressed homogeneously throughout the BLA or showed high expression in nearby brain regions were not selected (Extended Data Fig. 1G). Some of the selected genes were strongly enriched in one cluster, including *Sema5a* (cl5), and *Grik1* (cl12), while others were enriched in two or more clusters, including *Rorb* (cl7,8), *Otof* (cl2,3,6) and *Lypd1* (cl2,8,9) (Fig. 1F). By this analysis, every cluster of glutamatergic BLA neurons could be represented by a combination of one to four marker genes (Fig. 1E, F). This approach provided a combinatorial set of marker genes for spatial mapping of molecularly-defined glutamatergic BLA cell types.

Spatial organization of glutamatergic BLA clusters

For spatial mapping of glutamatergic BLA clusters, we performed sequential multi-plexed fluorescent in situ hybridization (smFISH) from anterior to posterior whole BLA coronal sections (Extended Data Fig. 2-3). We used four coronal sections — designated “anterior”, “anterior-middle”, “posterior-middle” and “posterior” — to divide the BLA into eight subregions from anterior to posterior (aLA, pLA, ppLA, amBA, alBA, acBA, pBA, ppBA) according to published methods [51](Fig. 2A-D). The numbers of cells positive for each marker gene were counted and the fractions of positive cells in each subregion were analyzed (Fig. 2E, see Methods). Briefly, we set a threshold on the fluorescence signal of each marker gene to determine whether a cell was positive or negative for a particular marker and then calculated the percentages of positive cells for each gene within each subregion. Since some cells were positive for multiple markers, the sum of cell fractions per subregion exceeded 100%. This analysis also allowed us to compare cell abundance across the different subregions. The results indicated that the clearest distinction was between LA and BA. For example, *Rorb*-positive cells were enriched in LA and less frequent in BA subregions (Fig. 2A-E). *Etv1* and *Rspo2*-positive cells showed the opposite pattern (low in LA, high in BA), which was most obvious in anterior and anterior-middle sections (Fig. 2A, B). We also observed that cell distributions varied in the A-P axis. For example, *Cdh13* expression was nearly absent in aLA and enriched in pLA/ppLA, whereas *Rorb* was enriched in aLA and less so

in ppLA (Fig. 2A, D). Some patterns were more complex: *Lypd1*-positive cells were enriched in the whole LA and several parts of the BA (Fig. 2A-E). *Grik1*-positive cells were scarce in the most anterior sections and enriched in posterior parts of LA and BA (Fig. 2C, E).

Next, we asked if the pattern of cell distribution based on the expression of the ten marker genes would be sufficient to delineate subregions of BLA. Pearson correlation revealed that LA and BA separated clearly, which could be further subdivided in the A-P axis, separating aLA from pLA/ppLA, and amBA/alBA from the more posterior acBA/pBA/ppBA (Fig. 2F). These results indicate that cells with similar expression profiles were distributed in distinct patterns in BLA subregions.

The combination of marker genes predicts the spatial localization in the BLA

During the above analysis, we noticed that the distribution of cells did not always follow the boundaries of the subregions, raising the possibility that subregions could be further subdivided or arranged differently. For example, *Otof*-positive cells were highly concentrated at the lateral edge of the alBA and rather scarcely present in the rest of the alBA (Fig. 2A) and *Cdh13*-positive cells were enriched at the tip of pLA (Fig. 2C). Since every cell was characterized by a unique combination of marker genes and its unique space within the BLA, we next asked in an unsupervised way, whether cells with a similar combination of marker genes would localize to a similar subregion of the BLA. For this, we used principal component analysis (PCA) to examine the variation of cells with their unique marker gene combinations and re-constructed the spatial localization of each PC back into the BLA. As the eigen-images from the top 4 PCs explained on average 80.8 ± 5.16% of variance in each sample, four PCs were enough to represent the variance. The results indicated that the PC associated with the largest variation in gene expression corresponded to differences between LA and BA (Extended Data Fig. 4). PCA also revealed that the markers *Etv1*, *Rspo2* and Lypd1 had large loadings in the top 4 PCs that

184 demarcate the boundary between LA and BA. For example, *Etv1* and/or *Rspo2*-positive cells
185 contributed most to BA-specific PCs (Extended Data Fig. 4 A1, B2, C2, D2), while *Lypd1*-positive
186 cells contributed most to LA-specific PCs (Extended Data Fig. 4 B3, C3, D3, D4). Also, *Cdh13*-
187 positive cells contributed to LA-specific PCs (Extended Data Fig. 4 B1, C3, D4). In summary, our
188 findings suggest that cells with a similar combination of marker genes localized to similar
189 subregions of the BLA. Moreover, the expression patterns of *Etv1, Rspo2* and *Lypd1*, parcellated
190 the BLA into its LA and BA subdomains. These results show that genetically-marked cell
191 populations distribute in distinct BLA subregions when analyzed in an unsupervised way.

192 To enhance the reliability of our transcriptomic and spatial expression analyses, we conducted a
193 side-by-side comparison on expression correlation of marker genes in snRNAseq and smFISH,
194 respectively. In terms of transcriptional profiles, *Etv1*, *Bdnf*, *Adamts2*, and *Rspo2* exhibited a
195 strong correlation and clearly separated from the other genes (Extended Data Fig. 5A). An
196 analogous analysis using smFISH data revealed a similar trend: *Etv1*, *Bdnf*, *Adamts2*, and *Rspo2*
197 were tightly correlated and predominantly found in the anterior BA (Extended Data Fig. 5B).
198 Notably, the correlation trends remained consistent throughout. *Otof*, *Lypd1*, and *Cdh13*
199 consistently showed close correlations and were primarily expressed in the posterior LA, while
200 Sema5a and Grik1 were closely correlated and appeared predominantly in the posterior BA
201 (Extended Data Fig. 5A, B).

202

203 **Transcriptional clusters with distinct expression patterns in BLA subregions**

204 Until now, we used the data from smFISH to assign each cell to a specific BLA subregion. Next,
205 we assigned each transcriptomic cell cluster to a space in the BLA in an unsupervised way using
206 Pearson correlation analysis. Since every cell belonged to a transcriptomic cell cluster and, in
207 addition, was characterized by the smFISH read counts of ten marker genes, we could calculate
208 the scaled sums of expression of the ten marker genes for each cluster (Extended Data Fig. 6A).

For example, cluster 2 was characterized by high expression of *Sema5a*, *Otof*, *Lypd1* and *Cdh13* (0.96-1.0) and lower expression of *Etv1* (0.63) and *Rspo2* (0.47).

In the smFISH data, every cell was characterized by the normalized expression of ten marker genes. We therefore correlated (Pearson) the smFISH marker expression pattern (Extended Data Fig. 6A) to each transcriptomic cluster marker expression pattern and assigned each smFISH cell to one of the 11 clusters according to the highest correlation coefficient (Extended Data Fig. 6B). For example, one smFISH cell (Cell ID # 3234) with high *Etv1* expression had highest correlation coefficient with cl4 (R: 0.46) and was therefore assigned as cl4. Another smFISH cell (cell ID # 1936) with high *Rspo2* expression showed higher correlation coefficient to cl11 (R:0.46), while a cell (cell ID # 5065) with high *Lypd1* expression showed higher correlation coefficient to cl2 (R: 0.71) (Extended Data Fig. 6B). After the assignment of all smFISH cells to individual transcriptional clusters, all cells were reconstructed into BLA space by using the spatial coordinates from smFISH (Extended Data Fig. 6C). For example, cl1, and cl11 were enriched in anterior BA, cl4 more posterior BA (Fig. 3A). These three clusters were characterized by high expression *Rspo2* and *Etv1*. Instead, cl2 and cl8 were enriched in pLA or ppLA (Fig. 3A) and were characterized by high expression of *Lypd1*. cl7 was enriched in anterior LA and was characterized by high expression of *Rorb*. By this analysis, transcriptomic clusters could be annotated to BLA subregions. (Fig. 3B).

Using average expression of the ten marker genes for each cluster we analyzed the correlation between clusters and generated a dendrogram (Fig. 3C). We annotated the tree with BLA subregions from the above analysis. Those clusters localized to LA correlated better compared to BA clusters. And in each branch of the tree, clusters separated according to their A-P axis. (Fig. 3C). In summary, these results from unsupervised analysis suggest that transcriptional cell clusters of glutamatergic neurons distribute in distinct BLA subregions. In the D-V axis, there is a

clear separation of cell clusters, while in the A-P axis we find both segregated clusters, but also gradual expression changes.

Genetically- and spatially-defined neurons show different response properties

We selected three genetic markers for functional analysis. *Lypd1*, the marker with highest expression in LA and additional regions in BA, targeting three transcriptomic clusters (cl2,8,9); *Etv1*, the marker with scarce expression in LA, complementary pattern with *Lypd1* in BA subregions, targeting three clusters (cl1,4,9); *Rspo2*, scarce expression in LA, restricted pattern in anterior BA, partially overlapping with *Etv1*, targeting two clusters (cl1,10). Among these markers, only Rspo2 had previously been analyzed functionally and will serve as a reference for comparison [3]. A comparative mRNA expression analysis revealed that *Lypd1*-expressing cells showed little overlap with *Etv1*- or *Rspo2*-expressing cells (typically less than 20% overlap, Extended Data Fig. 7A-C). *Etv1*- and *Rspo2*-expressing cells overlapped strongly in anterior sections (55%) and much less in posterior sections (30%) (Extended Data Fig. 7C). The fraction of *Lypd1*-expressing cells increased from anterior to posterior, while those of *Rspo2*- and *Etv1*-expressing cells decreased from anterior to posterior.

To analyze the intrinsic physiological properties of the neurons marked with the three selected genes, we used the respective Cre lines, Lypd1-Cre, Etv1-CreER, and Rspo2-Cre, and validated Cre expression in comparison to the endogenous markers (Extended Data Fig. 8). We crossed the Cre lines to a tdTomato reporter line and performed ex vivo electrophysiology in brain slices. Whole cell current-clamp recordings revealed significant differences in the membrane potentials with BLA^{Lypd1} neurons showing the most negative and BLA^{Rspo2} neurons the least negative (Fig. 4A), suggesting that BLA^{Lypd1} neurons may require more excitatory inputs to fire than the other two. Basic firing rates did not differ between cells (Figure S9A); however, spontaneous excitatory postsynaptic currents (sEPSC) had a lower amplitude and spontaneous inhibitory postsynaptic

currents (sIPSC) had lower frequency in BLA^{Lypd1} than BLA^{Rspo2} cells (Extended Data Fig. 9B), suggesting that BLA^{Lypd1} cells express fewer glutamate receptors and receive fewer inhibitory inputs.

Since part of our analysis involved appetitive behavior, which is known to be controlled by BLA neurons [1,3], we asked if overnight fasting would modify neuronal activities. Current-clamp recordings showed that the firing rates of BLA^{Lypd1}, but not BLA^{Etv1} neurons, increased in fasted mice and their membrane potentials depolarized (Fig. 4B-F). This suggests that fasting increased the excitability of BLA^{Lypd1} neurons. Recordings of excitatory and inhibitory neurotransmission revealed increased frequencies of sEPSC and sIPSC in BLA^{Lypd1} neurons after fasting (Fig. 4G-I). Additionally, the decay time for sEPSC decreased in BLA^{Lypd1} neurons after fasting, suggesting changes in the kinetics of the excitatory receptors (Fig. 4J). Other electrophysiological parameters measured in BLA^{Lypd1} neurons did not change after fasting (Extended Data Fig. 9C). Together these results suggest that the physiological properties of BLA^{Lypd1} neurons change during periods of energy deficits.

To understand how these BLA neuron populations modulate appetitive and defensive behaviors, we performed single-cell-resolution *in vivo* calcium imaging in freely moving mice. A graded-index (GRIN) lens was implanted above the BLA in the respective Cre lines previously injected with an AAV expressing a Cre-dependent GCaMP6f calcium indicator (Extended Data Fig. 9F). Calcium activity was monitored with a head-mounted miniaturized microscope in a free feeding assay [52] (Fig. 4K). We quantified mouse feeding behavior according to their approach behavior towards food rather than food consumption, because in previous work on central amygdala neurons, the presence of food correlated better with neuron activity than food consumption [53]. In order to visually inspect the correlation between the neural activities and the distance to food, we plotted the firing rate inferred from the calcium traces (see Methods for details) with the behavior trace (Fig. 4L). We observed many neurons with substantially high firing rates in specific areas. In some

283 of these neurons, these high firing rate areas partially overlapped with the location of the food
284 container, while we observed the opposite in other neurons (Fig. 4L). To quantitatively assess the
285 relationship between firing rate and the distance to food, we used spike detection to deconvolve
286 calcium traces, divided the distance to food into 31 bins, and computed the average firing rate at
287 each distance bin for each neuron. The area in which we observed feeding behavior, was within
288 a 5 cm radius around the food container and was termed the pro-food area. The area in which no
289 approach towards food was observed, was outside a 17 cm radius around the food container and
290 was termed the anti-food area. The area in-between was termed neutral area (Fig. 4L-N). For
291 each neuron, we determined the peak firing rate, which was then used to sort the neuron into pro-
292 food, neutral, or anti-food areas (Fig. 4M, N). We also performed a permutation test to identify the
293 neurons whose activity was significantly correlated with the distance to food (see method for
294 details). In brief, we computed the null distance distribution after shuffling the spike train for each
295 neuron and determined if the neuron was considered significantly tuned to distance to food
296 (termed “significant neurons”), by calculating if the maximum average firing rate of the distance
297 distribution of a neuron was higher than 95% of the null distribution (Fig. 4N, O). This analysis
298 revealed that the food-distance sorting pattern of the significant neurons was consistent with the
299 pattern of all neurons (Fig. 4M-O).

300 The quantification of all neurons revealed that the largest fraction of active neurons in the BLA^{Lypd1}
301 population was in the pro-food area (40.8%) (Fig. 4P). This percentage value was statistically
302 significant, when we computed the null percentage distribution of all pooled neurons from the 3
303 populations (shuffled data), randomly selected N neurons (N equals the number of neurons in the
304 tested population), and compared the percentage of recorded data with the shuffled data (Fig. 4P,
305 left). Consistently, the percentage of BLA^{Lypd1} significant neurons in the pro-food area was
306 significantly higher than chance level in comparison with the shuffled data of significant neurons
307 from all three populations (Fig. 4P, right). This was in contrast to the BLA^{Etv1} population, where

only the anti-food fraction in the significant neurons was larger than chance level (Fig. 4Q, right). In case of BLA^{Rspo2} neurons, the fractions of active cells in the neutral area across both all and significant neurons were larger than chance level (Fig. 4R). The averages of food consumption for recorded mice were similar across Cre lines (Extended Data Fig. 9H). These findings confirmed that the representation of neuronal activities according to distance-based food preference is statistically reliable and further revealed that BLA^{Lypd1} neurons were activated during fasting and food approach behavior.

BLA^{Etv1} neurons are activated by innate fear stimuli

In previous work, BLA^{Rspo2} neurons were activated by electric footshocks during contextual fear conditioning (CFC) [8]. We therefore asked, what fractions of BLA^{Lypd1} and BLA^{Etv1} neurons were activated by these negative valence stimuli. On day 1 of CFC, we recorded neuronal activities during footshocks and compared the firing rates (FR) during the 2 sec before and during footshocks (Fig. 5A). Then, we calculated the shock response scores (SRC, see Methods) for each neuron with scores of 1.0 and -1.0 being maximally activated and inhibited, respectively (Fig. 5B-C). To classify footshock-positive responsive neurons (pro-footshock) or footshock-negative responsive neurons (anti-footshock), we generated a null SRC distribution from the mean SRC for each shuffled spike train (see method for details). A neuron whose mean SRC was larger than the top 2.5% of the null SRC distribution was considered pro-footshock and a neuron with a mean SRC lower than the bottom 2.5% of the null distribution was considered anti-footshock neuron. This analysis revealed that the fraction of pro-footshock neurons was much larger in the BLA^{Etv1} population (42.2%) than in the BLA^{Lypd1} population (28.6%) (Fig. 5C).

On day 2 of CFC, we monitored the contextual freezing response, which was similar between the two populations of mice (Extended Data Fig. 9I). When we correlated the frequency of freezing of individual mice with the percentage of pro-footshock neurons on day 1, we found a positively correlated trend in the BLA^{Etv1} population, but not in the BLA^{Lypd1} population (Fig. 5D). These

results indicate that a sizeable fraction of BLA^{Etv1} neurons was activated by innate fear stimuli and raise the possibility that the fraction of pro-footshock neurons contributes to the conditioned freezing response.

Activities of BLA^{Etv1} neurons increase during social interactions

Next, we examined whether these three neuron populations were modulated by social interactions, a type of appetitive behavior that was previously shown to be regulated by the BLA but was not associated with a specific neuron population [1,39,44]. We confronted individual mice with a younger conspecific of the same gender in a wired container, either in a round cage or a two-compartment chamber (Fig. 5E). Social behavior was quantified as the approach behavior towards the other mouse using data from both chambers. The area in which we observed social interactions, was within a 10 cm radius around the center of the wired container and was termed the “pro-social area”. The area in which no approach behavior or social interactions occurred was outside a 20 cm radius around the wired container and was termed the “anti-social area”. The area in-between was termed neutral area (Fig. 5E). Similar to the analysis of neuronal activity during food approach, we performed permutation tests to identify the neurons whose activity was significantly correlated with the distance to the social interaction partner and found that the social-distance sorting pattern of the significant neurons was consistent with the pattern of all neurons (Fig. 5G-I).

The quantification of all neurons revealed that the smallest fraction of active BLA^{Lypd1} neurons was in the pro-social area (24.6%), both for all and significant neurons (Fig. 5J), and this percentage value was significantly lower than chance level in comparison with the shuffled data of significant neurons from all three populations (Fig. 5J, right). Interestingly, the largest fraction of active neurons in the BLA^{Etv1} population was in the pro-social area (42.6%) and this percentage value was significantly higher than chance level (Fig. 5K). In contrast, the percentages of active BLA^{Rspo2} neurons did not change in this social interaction assay (Fig. 5L). Total distance moved

357 during social tasks were similar across Cre lines (Extended Data Fig. 9J). These results indicate
358 that BLA^{Etv1} neurons were activated during social interactions.

359

360 **BLA^{Lypd1} neurons are positive valence neurons and promote normal food uptake**

361 The activation patterns of these BLA neurons suggested that they participated in valence-specific
362 behaviors. We first asked, if optogenetic activation of these populations would be sufficient to
363 promote appetitive behavior. We also employed optogenetic inhibition approaches to investigate,
364 if one or more of these populations would be necessary to mediate appetitive behavior. We
365 expressed channelrhodopsin-2 (ChR2) in all three Cre lines using a Cre-dependent viral vector
366 (AAV5-Ef1α-DIO-hChR2(H134R)-EYFP) bilaterally targeted to the BLA and implanted optical
367 fibers bilaterally over the BLA for somata photostimulation (Fig. 6A, B). Control mice received a
368 similar AAV vector lacking ChR2 (AAV5-Ef1-DIO- EYFP). The feeding assay was the same as
369 the one used for calcium imaging. Food consumptions during light-On and light-Off phases were
370 measured on separate days using the same cohorts of mice. After 20h of fasting, photoactivated
371 Lypd1-Cre::ChR2 mice consumed significantly more food than EYFP control mice and in
372 comparison to Light-off days (Fig. 6C). This was in contrast to Etv1-CreER::ChR2 and Rspo2-
373 Cre::ChR2 mice, which consumed significantly less food during the Light-On compared to the
374 Light-Off phase (Fig. 6C). The observed effects were independent of general locomotor behaviors
375 (Extended Data Fig. 10A). To acutely photoinhibit neurons, we expressed Cre-dependent
376 Halorhodopsin (eNpHR3.0-mCherry) in a similar fashion as ChR2 and assessed food
377 consumption. We found that photoinhibited, hungry Lypd1-Cre::eNpHR mice ate significantly less
378 food than in the absence of photoinhibition (Fig. 6D), while the same manipulation had no effect
379 on Etv1-CreER::eNpHR and Rspo2-Cre::eNpHR mice. In summary, the activity of BLA^{Lypd1}
380 neurons is both sufficient and necessary to promote feeding. Activation of BLA^{Etv1} or BLA^{Rspo2}

neurons can suppress feeding. However, these neurons may not be required for food uptake in the free-feeding assay.

We also assessed the intrinsic valence of optogenetic activation of the three types of BLA neurons in the neutral environment of a conditional place preference assay (CPP) (Fig. 6E, see Methods). After conditioning, Lypd1-Cre::ChR2 mice exhibited a significant preference for the photostimulation-paired chamber, whereas Etv1-CreER::ChR2 and Rspo2-Cre::ChR2 mice showed significant avoidance behavior for the photostimulation-paired chamber (Fig. 6E). No changes in anxiety were observed in Open-Field behavior (Fig.S10B). These results indicate that mice can learn to associate an open area with positive valence for photoactivation of BLA^{Lypd1} neurons and conversely, with negative valence for photoactivation of BLA^{Etv1} or BLA^{Rspo2} neurons.

BLA^{Etv1} neurons are necessary for fear memory formation

Given that BLA^{Etv1} neurons were strongly activated by footshocks, we next asked if optogenetic manipulation of these neurons would affect the freezing response in a CFC experiment. On day 1 of CFC, footshocks were paired with either photoactivation or photoinhibition of the somata of BLA^{Etv1} or BLA^{Lypd1} neurons (Fig. 7A, B). On day 2 (Fear recall), the fraction of time the animals spent freezing was monitored. Photoactivation of Lypd1-Cre::ChR2 mice resulted in significantly less freezing than photoactivation of EYFP control mice, while similar levels of freezing were observed in Etv1-CreER::ChR2 mice compared to their respective EYFP control mice (Fig. 7A). Conversely, photoinhibition of Etv1-CreER::eNpHR mice resulted in significantly less freezing on fear recall day compared to their respective mCherry control mice, while similar levels of freezing were observed in Lypd1-Cre::eNpHR mice compared to Lypd1-Cre::mCherry control mice (Fig. 7B). The reduction in freezing of photoinhibited Etv1-CreER::eNpHR mice could already be observed during fear acquisition (day 1) (Extended Data Fig. 10D). These results showed that

405 BLA^{Etv1} neurons are necessary for fear memory formation. They further indicate that BLA^{Lypd1}
406 neurons are sufficient to suppress freezing behavior.

407

408 **BLA^{Etv1} neurons are necessary for social interaction**

409 Given that a large fraction of BLA^{Etv1} neurons were activated during social behavior, we next
410 asked, if optogenetic manipulation of these and other neurons would alter social behavior. Social
411 behavior assays were performed as for calcium imaging experiments. Interestingly,
412 photoactivation of Etv1-CreER::ChR2 mice resulted in mice spending more time in the social zone
413 compared to the light-off phase, an effect that was not observed in control mice expressing YFP
414 (Fig. 7C). Instead, interactions of photoactivated Etv1-CreER::ChR2 mice with the empty cage
415 were unaffected (Extended Data Fig. 10E). The converse effect was observed in photoinhibited
416 Etv1-CreER::eNpHR mice which spent significantly less time in the social zone compared to the
417 light-off phase (Fig. 7D). Neither optogenetic manipulation of BLA^{Lypd1} nor BLA^{Rspo2} neurons
418 altered their social behavior, which was in line with the observed neutral responses in the calcium
419 imaging experiments. Together, these results showed that BLA^{Etv1} neurons encoded sociability
420 and were sufficient and necessary to drive social interaction.

421

422 # Discussion

423 In this report, we have described a full single cell transcriptomic analysis of glutamatergic neurons
424 in the BLA of adult mice. In combination with smFISH, we characterized a total of 11 cell clusters
425 and demonstrated that they distributed in distinct spatial BLA subregions. Several clusters
426 showed a clear preference between LA and BA, other clusters were enriched in either anterior or
427 posterior regions of the BLA. We selected three genetic markers for functional analysis. *Lypd1*,

the marker with highest expression in LA and additional regions in BA, targeting three transcriptomic clusters (cl2,8,9); *Etv1*, the marker with scarce expression in LA, complementary pattern with *Lypd1* in BA subregions, targeting three clusters (cl1,4,9); *Rspo2*, scarce expression in LA, restricted pattern in anterior BA, partially overlapping with *Etv1*, targeting two clusters (cl1,10). We found that BLA^{Lypd1} neurons are positive-valence neurons: they are activated during fasting and food approach behavior, and mediate normal food uptake. BLA^{Etv1} neurons are mixed-selectivity neurons: they are activated by innate fear stimuli and during pro-social approach behavior. They promote the formation of fear memory and promote social interactions. BLA^{Rspo2} neurons are negative-valence neurons: BLA^{Rspo2} match the idea of a typical aversive population by not responding to neither food nor social cues and promoting aversive conditioning. Together these findings describe the rich diversity of glutamatergic cell types and their spatial distribution in the BLA, support the concept that genetically-defined subpopulations respond either to valence-specific or mixed cues, and expand their behavioral output to the promotion of normal feeding and social behavior.

Our single nuclei transcriptomics analysis provides an extensive account of glutamatergic cell clusters. The results matched with previously published work [14] based on Seurat::IntegrateData. For example, cluster 8: (Rorb/Lypd1) which was enriched in anterior LA, showed similarity with O'Leary et al.'s LA1 subpopulation (Extended Data Fig. 11A, B). Cluster 2, (Sema5a/Otof/Lypd1/Cdh13) which localized to posterior LA, matched mainly with O'Leary et al.'s LA2 subpopulation (Extended Data Fig. 11B). Compared to LA, the BA clusters matched less well. Cluster 3 (Otof) which localized to posterior BA, matched with O'Leary et al.'s BA2 subpopulation [14]. However, cluster 1 (Rspo2/Etv1/Adamts2/Bdnf), which localized to the whole anterior-posterior extent of the BA, was included in all O'Leary et al.'s BA1-BA4 [14]. Importantly, our most anterior and most posterior located clusters did not match, suggesting that the very anterior and very posterior extents of the BLA were not included in the O'Leary dataset [14] (Extended Data Fig. 11B).

We also compared our data with the recent comprehensive transcriptomic and spatial atlas of cell types in the whole mouse brain [54] . To our surprise, the whole brain atlas did not reveal different cell clusters in BLA, suggesting that this approach may not have enough resolution to reveal sparse cell clusters.

Our characterization of BLA^{Rspo2} neurons corresponds well with previous work [3] in terms of their enrichment in the anterior BA and their function in negative-valence behavior. The same study characterized BLA^{Ppp1r1b} neurons enriched in the posterior BA as positive-valence neurons [3]. Our snRNAseq dataset did not include *Ppp1r1b*, which may either indicate low expression levels of this transcript as previously suggested [4] or limitations of snRNAseq in detecting certain low abundant mRNAs. *Fezf2*, another marker for valence-specific BLA neurons[4] was expressed rather widely in our snRNAseq dataset, including BLA^{Rspo2} neurons, and may represent a rather large fraction of BA neurons with functional heterogeneity.

The present study characterized distinct cell clusters in LA and BA which confirms the O'Leary et al. dataset [14], and is consistent with the LA having a distinct role from the BA in emotional learning [55]. Previous work indicated the presence of continuous spatial gene-expression gradients [3,14,56], rather than distinct cell clusters that are positioned in specific spatial locations. We used two different methods to assign spatial locations to cell clusters. First, we assigned 10 specific marker genes to represent all cell clusters and delineated their expression within eight previously published subregions using smFISH. Second, we used the smFISH data to map every cell belonging to a specific transcriptional cluster to BLA space in an unsupervised manner. Using both methods we find evidence for both scenarios, clusters with graded variability (e.g. cluster 1: (Rspo2/Etv1/Adamts2/Bdnf) in BA) and clusters showing more distinct spatial locations (e.g. cluster 3: (Otof), no expression in aBA, high in pBA, or cluster 7: (Rorb,) high in aLA, no expression in pLA.

Our functional analysis revealed the presence of a previously uncharacterized BLA^{Lypd1} neuron population as positive-valence neurons. BLA^{Lypd1} neurons are found in three cell clusters in LA and acBA, complementary to BLA^{Etv1} neurons which are enriched in amBA and alBA. In slice electrophysiological recordings, BLA^{Lypd1} neurons showed increased firing rates in fasted animals, similar to our previous recordings of appetitive CeA neurons [57]. *In vivo* calcium recordings revealed that a large fraction of BLA^{Lypd1} neurons are active during food approach behavior, whereas smaller fractions of BLA^{Lypd1} neurons respond to fear and social stimuli. Optogenetic manipulations demonstrated that BLA^{Lypd1} neurons are both sufficient and required for normal food uptake. These results are surprising in light of previous work indicating that the BLA does not promote free-feeding behavior [33,34], and that it has a negative effect on food consumption in a risky environment [35]. The main difference to previous work is that we have manipulated a distinct subpopulation, enriched in LA and certain parts of BA, whereas previously either most of the BA or certain BLA projections had been manipulated. Hence, BLA^{Lypd1} neurons may have largely been left untouched in previous manipulation experiments. A role of BLA PN in promoting normal feeding is supported by studies that had shown that BLA neurons are responsive to a variety of foods [8,36]. The positive valence function of BLA^{Lypd1} neurons is not restricted to feeding, since mice can be conditioned to associate a positive valence with photoactivation of BLA^{Lypd1} neurons in a CPP assay and since the photoactivation of BLA^{Lypd1} neurons suppresses the formation of fear memory. The function of these neurons is, however, not to enhance any ongoing motivated behavior, since BLA^{Lypd1} neurons did not modulate social interactions. The mechanism by which BLA^{Lypd1} neurons promote food intake remains to be explored. It is possible that BLA^{Lypd1} neurons directly synapse onto orexigenic CeA neurons including the recently described Ghrelin-responsive CeA^{Htr2a} neurons [57]. It also remains to be tested whether the activity of BLA^{Lypd1} neurons is modulated by other internal states besides hunger and by environmental factors such a risk stimulus [35]. It may be interesting for human studies to investigate BLA's role in prevalence of maladaptive eating behaviors in humans.

While BLA^{Lypd1} neurons are mainly positive-valence neurons, BLA^{Etv1} neurons show mixed selectivity and are activated by aversive cues (foot shock) and during social interactions, but not during fasting or by the presence of food. This observation supports previous studies showing that BLA neurons can respond to multiple stimuli, including social and non-social cues [58–62]. Interestingly, BLA^{Etv1} neurons are a newly described BLA population that is activated by aversive and social cues. In line with the calcium imaging data, our optogenetic manipulation experiments revealed that BLA^{Etv1} neurons promote defensive behavior (contextual fear memory formation and conditional place aversion) and social interactions. The presence of negative valence BLA neurons is not novel, as this has previously been shown in several labs [5,6,63–65]. However, the presence of neurons promoting both defensive and social behavior is surprising, considering that most of previous evidence suggested that the BLA mediates aversive aspects of social interaction [40,44]. A recent report paints a more detailed picture by showing that medial prefrontal cortex to BLA subcircuits regulate social preference in a bi-directional manner. While prelimbic cortex (PL) -BLA projectors suppress, infralimbic cortex (IL) -BLA projectors were required for social interactions [66]. These results raise the interesting possibility that the target neurons of IL-BLA projectors may be BLA^{Etv1} neurons. A recent study identified a subpopulation of BLA PN expressing secretin (SCT) as promoters of social behavior[39] indicating the presence of distinct subsets of BLA neurons facilitating social interactions. Whether BLA^{SCT} neurons overlap with BLA^{Etv1} neurons and whether they also promote fear memory formation remains to be investigated.

The circuits regulating social interactions are likely very complex and are not well understood. Having access to genetically-defined subpopulations of BLA neurons that are integrated in these circuits will greatly accelerate the process of social circuit dissection. Similar to the regulation of food consumption, social behavior and the underlying amygdala circuits are evolutionarily conserved. Their examination in different animal models and humans will ultimately benefit our understanding of the circuit basis of psychiatric disorders.

METHODS

Animals

Experiments were performed using juvenile mice (postnatal 10 days and 21 days) and adult mice (> 8 weeks). The wild-type animals were from the C57BL/6NRj strain (Janvier Labs). The Rspo2-Cre transgenic line (C57BL/6J-Tg(Rspo2-cre)BIto (RBRC10754)) from RIKEN BioResource Research Center) and Etv1-CreER transgenic line (Etv1tm1.1(cre/ERT2)) from Jackson Laboratory) and Lypd1-Cre (Tg(Lypd1-cre)SE5Gsat/Mmucd) mice were imported from the Mutant Mouse Regional Resource Center). Td-Tomato Rosa26R mouse lines were as described previously[67], using the line Ai9lsl-tdTomato [B6.Cg-Gt(ROSA)26SorTM9.CAG-tdTomato/Hze/J][68]. Transgenic mice were backcrossed with a C57BL/6N background. Animals used for optogenetic manipulations and calcium imaging were handled and singly housed on a 12 h inverted light cycle for at least 5 days before the experiments.Mice were given ad libitum food access except during food deprivation for feeding experiments. All behavior assays were conducted at a consistent time during the dark period (2 p.m.–7 p.m.). Both male and female mice were used and all the experiments were performed following regulations from the government of Upper Bavaria.

Viral constructs

The following adeno-associated viruses (AAVs) were purchased from the University of North Carolina Vector Core (https://www.med.unc. edu/genetherapy/vectorcore): AAV5-ef1a-DIO-eNpHR3.0-mCherry, AAV5-hSyn-DIO-mCherry, AAV5-Ef1α-DIO-hChR2(H134R)-EYFP, AAV5-Ef1a-DIO-eYFP. The AAV5.Syn.Flex.GCaMP6f.WPRE.SV40 virus was obtained from Addgene.

SnRNA-seq

Single-nucleus RNA sequencing was focused on the basolateral amygdala (BLA). For visually guided dissection of the BLA, we practiced by using the fluorescent expression in basal amygdala (BA) of Rspo2-cre; tdTomato mice [3] and dense fiber tracks surrounding BLA boundaries to facilitate complete microdissection of BLA. Each single nucleus sequencing dataset includes BLA tissues from 4 male brains (both hemispheres). To reduce potential batch effects, brains were always from the same litter, collected and processed in parallel at the same time. Mice were deeply anesthetized by i.p. injections of 200 mg/kg Ketamine and 40 mg/kg Xylazine, and perfused with 10 mL ice-cold Sucrose-HEPES Cutting Buffer containing (in mM) 110 NaCl, 2.5 KCl, 10 HEPES, 7.5 MgCl2, and 25 glucose, 75 sucrose (~350 mOsm/kg), pH=7.4 [69]. All the solutions/reagents were kept on ice in the following procedures unless otherwise specified. The brain was extracted and cut (300 μm) on a vibratome (Leica VT1000S, Germany) in cutting buffer, and the slices were transferred into a Dissociation Buffer containing (in mM): 82 Na2SO4, 30 K2SO4, 10 HEPES, 10 glucose and 5 MgCl2, pH=7.4 [69]. BLA was microdissected under a microscope (Olympus SZX10) covering the anterior (Bregma −0.59) and posterior (Bregma −3.0) extent of the adult BLA.

Single nucleus isolation and library preparation

The protocol for single nucleus isolation was optimized from previous studies [70,71] and demonstrated nucleus isolation protocol (CG000393, 10x Genomics). In brief, collected tissue chunks from the four brains were transferred in 600 μl homogenization buffer containing 320 mM sucrose, 5 mM $CaCl_2$, 3 mM Mg $(CH_3COO)_2$, 10 mM Tris HCl pH 7.8, 0.1 mM EDTA pH 8.0, 0.1% NP-40 (70% in H_2O, Sigma NP40S), 1 mM β-mercaptoethanol, and 0.4 U/μl SUPERase RNase inhibitor (Invitrogen AM2694). The homogenization was performed in a 1mL Wheaton Dounce tissue grinder with 20 strokes of loose and then 20 strokes of a tight pestle. The homogenized tissue was filtered through a 20-μm cell strainer (Miltenyi Biotec) and mixed with an equal volume of working solution containing 50% OptiPrep density gradient medium (Sigma-Aldrich), 5 mM $CaCl_2$, 3 mM Mg $(CH_3COO)_2$, 10 mM

Tris HCl pH 7.8, 0.1 mM EDTA pH 8.0, and 1 mM β-mercaptoethanol. The resulting solution was transferred into a 2 mL centrifuge tube. A 29% OptiPrep density gradient solution including 134 mM sucrose, 5 mM $CaCl_2$, 3 mM Mg $(CH_3COO)_2$, 10 mM Tris HCl pH 7.8, 0.1 mM EDTA pH 8.0, 1 mM β-mercaptoethanol, 0.04% NP-40, and 0.17 U/µl SUPERase inhibitor was slowly placed underneath the homogenized solution through a syringe with a 20G needle. In the same way, a 35% Density solution containing 96 mM sucrose, 5 mM $CaCl_2$, 3 mM Mg $(CH_3COO)_2$, 10 mM Tris HCl pH 7.8, 0.1 mM EDTA pH 8.0, 1 mM β-mercaptoethanol, 0.03% NP-40, and 0.12 U/µl SUPERase inhibitor was slowly laid below the 30% density. The nuclei were separated by ultracentrifugation using an SH 3000 rotor (20 min, 3000xg, 4 °C). A total of 300 µl of nuclei was collected from the 29%/35% interphase and washed once with 2 mL resuspension solution containing 0.3% BSA and 0.2 U/µl SUPERase in PBS. The nuclei were centrifuged at 300g for 5 min and resuspended in ~30 µl resuspension solution. Nuclei were stained with DAPI and counted. After manually determining the cell concentration using a hemocytometer, suspensions were further diluted to desired concentrations (300–700 nuclei/µl) if necessary. The appropriate final suspension contained 5000 nuclei and was loaded into the chip. Nanoliterscale Gel Beads-in-emulsion (GEMs) generation, barcoding, cDNA amplification, and library preparation were done using the Chromium Next GEM Single Cell 3' Reagent Kits v3.1 according to the manufacturer's protocol.

snRNA-Seq analysis

Sequence alignment and preprocessing

Prepared libraries were sequenced on Illumina NextSeq 500 (Mid and High Output Kit v2.5, Paired-end sequencing, 28bp-130bp). We used cellranger (version 7.0.1) to extract fastq files, align the reads to the mouse genome (10x genomics reference build MM10 2020 A), and obtain per-gene read counts. Subsequent data processing was performed in R using Seurat (version 4.1.3) with default parameters if not indicated otherwise. After merging the data, we normalized the data

(normalization.method='LogNormalize', scale.factor=10000), detected variable features (selection.method='vst', nfeatures=2000), and scaled the data (vars.to.regress=c('nCount_RNA'). We then applied quality control filters on cells with the following criteria: a) more than 200 genes detected, b) less than 20% mitochondrial gene reads, c) more than 5% ribosomal protein gene reads, d) less than 0.2% hemoglobin gene reads, e) singlets as determined by doubletFinder (version 2.0.3, pK = 0.09, PCs=1:10). Only genes detected in at least 4 cells were kept. The resulting dataset consisted of 7,953 cells and 21,557 genes. Initial cell clustering was performed with resolution 0.4 after applying harmony batch correction (version 0.1.1) and subsequent UMAP embedding on the harmony reduction.

Global annotation

For global annotation, non-neuronal clusters were identified by expression of non-neuronal markers (e.g., *Plp, Mbp, Pdgfra, Olig, Lhfpl3, Igfbp7, Bsg, Tmem119, Cst3, P2ry12, Hexb, C1qb, C1qa, Aldh1l1, Gfap, Slc1a2, Cfap299*) and absence of neuronal markers (*Snap25, Slc17a7, Slc17a6, Neurod6 Syp, Tubb3, Map1b, Elavl2, Gad1, Gad2*, etc.). Neuronal clusters were confirmed by expression of neuronal markers above and neurotransmitter and neuromodulator releasing neurons were annotated by well-known markers (glutamatergic neurons: *Slc17a7, Slc17a6, Camk2a, Gria2*, GABAergic neurons: *Adora2a, Gad1, Gad2, Gabbr1, Gabbr1, Gad65, Gad67).*

For annotation of GABAergic neurons in BLA, firstly only GABAergic neurons based on above global annotation were subtracted and re-clustered. Next, conventional markers from a previous study [72] were used (*Reln, Ndnf, Sst, Pvalb, Vip, Cck, Calb1, Crh, Npy, Foxp2, Htr2a)* Also, GABAergic neuron markers for central amygdala (CEA) [73] were used as reference *(Prkcd, Ppp1r1b, Tac2, Wfs1, Dlk1, Penk, Drd2, Drd1, Calcrl, Pdyn, Nts, Tac1).* We sorted out BLA local inhibitory interneuron from neighborhood regions (e.g., projecting inhibitory neurons in CeA,

based on *Pkcd, Drd1* and *Drd2*) [72,73] or intercalated cells (ITCs, based on *Foxp2* expression) or the amygdalostriatal area (based on *Rarb* expression) [74,75].

For clarity, we unified the naming of cell populations in the diverse conditions as follows: clusters from unsupervised clustering were named “Clusters”, cell populations containing multiple clusters were named “Category” or named differently.

Marker-gene selection for glutamatergic neurons for spatial validation (smFISH)

To annotate subtypes of glutamatergic neurons in BLA we retained only glutamatergic neurons and subjected them to re-clustering. Initially, marker genes were identified using presto::top_markers (n = 5, auc_min = 0.5, pct_in_min = 20, pct_out_max = 20). We then handpicked the most specific gene for each cluster. For clusters where no marker could be pinpointed, we turned to in situ hybridization (ISH) data from Allen brain atlas: mouse brain. Preference was given to genes that exhibited higher expression in the BLA than other regions and showed localized expression within BLA subregions. Based on these criteria, we selected 10 marker genes shown in Figure 1F. It is worth noting that other combinations of genes might also adequately represent these molecularly defined cell types.

Construction of Phylogenetic tree of glutamatergic neurons

Cell type tree was calculated by Seurat::BuildClusterTree on the aggregated expression of all genes using hierarchical clustering of the distance matrix by using Euclidean distance.

Comparison with published BLA data

Mouse BLA scRNA seq data:https://doi.org/10.6084/m9.figshare.c.5108165 from O’Leary dataset [76.] We obtained expression matrices for data set GSE148866 from GEO and cell annotation from O’Leary dataset [76] and constructed a Seurat object. Normalization,

scaling and UMAP embedding was performed as described above. We integrated the data with our own using Seurat::IntegrateData after selecting and subsequently finding integration anchors. Cell-to-cell mapping was performed using scmap (1.18.0) as described in https://biocellgen-public.svi.edu.au/mig_2019_scrnaseq-workshop/comparing-and-combining-scrna-seq-datasets.html after splitting the Seurat object in two SingleCellExperiment objects.

HCR sequential multi-fluorescent in situ hybridization

C57BL/6J mice (n = 6, 3 male, 3 female, > 8weeks) were anesthetized IP with a mix of ketamine/xylazine (100 mg/kg and 16 mg/kg, respectively) (Medistar and Serumwerk) and transcardially perfused with ice-cold phosphate-buffered saline (PBS), followed by 4% paraformaldehyde (PFA) (1004005, Merck) (w/v) in PBS. The brain was dissected and immediately placed in a 4% PFA buffer for 2 h at room temperature. The brain was then immersed in 30% RNase-free Sucrose (Amresco, 0335) in 1X PBS for 48 h at 4 degree until the brain sank to the bottom of the tube. The brain was then embedded in OCT and cryo-sectioned (15 mm thick) by harvesting coronal sections through the AP extent of BLA and stored at −80°C. At least three coronal section were selected for analysis within each of the anterior (−0.79 to −1.07 from bregma), anterior-middle (−1.23 to −1.55 from bregma), posterior-middle (−1.67 to −2.03 from bregma) and posterior (-2.15 to -2.45 from bregma) regions of the BLA.

The selected ten genes were targeted in four sequential HCR rounds. The probe sets (Molecular Instruments) were used as follows: *Sema5a, Grik1, Rorb* (Round 1); *Adamts2, Bdnf* (Round 2); *Cdh13, Otof* (Round 3*); Lypd1, Etv1, Rspo2* (Round 4). The order of rounds was shifted by sections in order to reduce the possibility of loss of RNA after washing steps [77]. In all rounds, the Rnu6 probe was co-applied and used as a nuclear marker. Sections were processed according to the sequential hybridization chain reaction (HCR) protocol as published previously [78]. In brief,

667 sections were fixed in 4% PFA at 4°C, dehydrated in serial ethanol washes, and treated with
668 RNAscope Protease IV (ACDBio). Sections were rinsed and hybridized overnight at 37°C with
669 probes targeting the first gene set. Sections were then washed, and probes were amplified with
670 fluorophores (Alexa 405,488, 546, and 647) overnight at room temperature. Next, sections were
671 washed, and autofluorescence was quenched using a Vector TrueVIEW Autofluorescence
672 Quenching kit (Vector labs cat: # SP-8400). Slides were cover-slipped with Prolong Gold antifade
673 Mounting Medium (Invitrogen) and allowed to cure at RT for 2 hours before imaging. After each
674 round of imaging, coverslips were removed, and sections were washed to remove mounting
675 medium. The probes were then digested with DNase I (Sigma cat# 4716728001), and the next
676 probe set was hybridized. Images were acquired with a Leica SP8 confocal microscope and a
677 20×/0.75 IMM objective (Leica).

678 **Data analysis for HCR**

679 **Spatial organization in the BLA**

680 Firstly, four images from 4 rounds were superimposed by landmark and serial strain registration.
681 Also, cell segmentation (based on Rnu6 expression) and thresholding fluorescence for positive
682 cell per each gene were performed and quantification for cells expressing a given gene was also
683 analyzed by HALO software (Indica Labs). Thresholding required to classify a given gene
684 positive/negative cell was chosen based on visual inspection but double-blind way. Next, we
685 referred to a recent anatomy paper [51] for subregion delineation and coronal section selection of
686 BLA. In order to represent the whole BLA, our dataset constituted four coronal sections (anterior,
687 anterior middle, posterior middle and posterior) and eight subregions (aLA, pLA, amBA, alBA,
688 acBA, pBA, ppBA, ppLA). To visualize gene expression, positive cells were reconstructed and
689 plotted in dot colorized by gene. Finally, percentage of positive cells for each gene was calculated
690 within individual eight sub-regions. We did not separate multiple gene positive cells. Therefore,

691 the sum of percentage per subregion is more than 100%. Lastly, we compared this percentage
692 across coronal section as well as across subregions in Figure 2. Pearson's cross-correlation and
693 clustering analysis was computed between BLA subregions and the average of each percentage
694 per gene. Density heatmap was plotted in a color-scale (red = 1 and blue = 0, normalized value
695 by the highest density area (=1)). To map smFISH and snRNA-seq data correlation, we computed
696 pairwise Pearson correlation with hierarchical clustering of 10 marker gene expression across all
697 glutamatergic neurons (snRNA data) and of average percentage of 10 marker gene positive cell
698 across eight sub regions of BLA (smFISH) (Fig S5).

699

700 **smFISH PCA clustering analysis**

701 Data including x,y position of positive cells expressing each gene were imported to a Python
702 workflow in which unsupervised principal component analysis (PCA) were simply customized from
703 the pipeline (EASI-FISH) described before [79]. In brief, Images containing expression patterns of
704 10 marker-genes were decomposed into principal components (PCs). The eigen-images from the
705 top 4 PCs explained on average 80.8 ± 5.16% of variance in each sample. PCA of the expression
706 patterns of 10 marker-genes were reconstructed and used to identify spatial patterns in BLA
707 orientation. As the pattern demarcating BLA by each PC component across different samples was
708 homogeneous, we only selected samples with this homogenous pattern of PCA to make
709 populational analysis. Therefore, PC loading values for each gene were averaged by different
710 coronal sections (total 16 PC variance, e.g., anterior PC1, anterior PC2 or anterior-middle PC1,
711 anterior-middle PC2 etc) and clustered by Pearson's correlation across genes. This analysis was
712 compared with the clusters from percentages of cells positive for 10 marker genes in eight
713 subregions of BLA in supervised manner.

714 **Correlation between smFISH and snRNA clusters**

For mapping clusters of snRNAseq data to smFISH signals and corresponding locations, we first aggregated the single nuclei read counts for each cluster for each gene that was used in smFISH (Fig.S6). We then correlated (Pearson) the smFISH expression data — normalized z-scores of 10 marker genes in a of radius 50 µm [77] — with each cluster expression pattern and assigned each smFISH cell to one of the 11 clusters according to the highest correlation coefficient.

Stereotaxic surgeries

Mice were anesthetized for surgery with isoflurane (1.5–2%) and placed in a stereotaxic frame (Kopf Instruments). Body temperature was maintained with a heating pad. A systemic anesthetic (carprofen 5 mg/kg bodyweight) was administered. Mice used in in vitro and in vivo optogenetic experiments were bilaterally injected with 0.4 µl of optogenetic or control virus in the BLA by using the following coordinates calculated with respect to the bregma: −1.8 mm anteroposterior, ± 3.25 mm lateral, −4.75 mm ventral for Lypd1-Cre mice, bregma: −1.5mm anteroposterior, ± 3.25 mm lateral, −4.8 mm ventral for Rspo2- and Etv-Cre mice. In the same surgery, mice used in optogenetic experiments were bilaterally implanted with optic fibers (200-µm core, 0.5 NA, 1.25-mm ferrule (Thorlabs)) above the BLA (−4.6 mm ventral). Implants were secured with cyanoacrylic glue, and the exposed skull was covered with dental acrylic (Paladur). Mice used in in vivo calcium imaging experiments were injected in the right BLA (coordinates as above) with 0.4 µl AAV-GCaMP6f virus. One week later, the microendoscope was implanted. To do so, a 0.8-mm hole was drilled in the skull above the BLA. Debris was removed from the hole, and a sterile 20-gauge needle was slowly lowered into the brain to a depth of −4.8 mm from the cortical surface to clear a path for the lens. The GRIN lens (GLP-0673; diameter, 0.6 mm; length, ~7.3 mm, Inscopix) was slowly lowered into the brain to −4.75 mm from the bregma by using a custom lens holder. The lens was secured in place with glue (Loctite 4305) and dental cement (Paladur). The exposed top of the lens was protected by a covering of a silicone adhesive (Kwik-cast). Approximately four weeks after lens implantation, the mice were assessed for observable GCaMP6 fluorescence.

The heads of the mice were fixed, and the top of the lens was cleaned of debris. The miniature microscope (Inscopix) with a baseplate (BLP-2, Inscopix) was positioned above the lens such that GCaMP6 fluorescence and neural dynamics were observed. The mice were anesthetized with isoflurane, and the baseplate was secured with dental cement (Vertise Flow). A baseplate cap (BCP-2, Inscopix) was left in place until imaging experiments. Expression in Etv1-CreER animals was induced by intraperitoneal injections of tamoxifen (150-200 µl, 10 mg/ml, dissolved in 90% cornoil and 10% ethanol) two days after surgery on 4 consecutive days in the modified way as described[80].

Acute brain slice preparation and electrophysiological recordings.

The animals were anesthetized with isoflurane and decapitated under deep anesthesia. The brain was immediately immersed in an ice-cold cutting solution consisting of NaCl (30 mM), KCl (4.5 mM), MgCl2 (1 mM), NaHCO3 (26 mM), NaH2PO4 (1.2 mM), glucose (10 mM), and sucrose (194 mM), equilibrated with a 95% O2/5% CO2 gas mixture. The brain was sectioned into slices of 280 µm thickness using a Leica VT1000S vibratome and transferred to an artificial cerebrospinal fluid (aCSF) solution containing NaCl (124 mM), KCl (4.5 mM), MgCl2 (1 mM), NaHCO3 (26 mM), NaH2PO4 (1.2 mM), glucose (10 mM), and CaCl2 (2 mM), equilibrated with 95% O2/5% CO2 gas mixture and maintained at 30-32°C for 1 hour before being returned to room temperature.

The brain slices were mounted in a recording chamber and perfused continuously with the aforementioned aCSF solution equilibrated with 95% O2/5% CO2 gas mixture at 30-32 °C. Whole-cell patch-clamp recordings were performed using patch pipettes prepared from filament-containing borosilicate micropipettes with a resistance of 5-7 MΩ. The intracellular solution used for recordings contained potassium gluconate (130 mM), KCl (10 mM), MgCl2 (2 mM), HEPES (10 mM), Na-ATP (2 mM), Na2GTP (0.2 mM) and had an osmolarity of 290 mOsm. The brain slices were visualized using an IR-DIC equipped fluorescence microscope (Olympus BX51) and

764 data were acquired using a MultiClamp 700B amplifier, a Digidata 1550 digitizer, and analyzed
765 using the Clampex 10.3 and Clampfit software from Molecular Devices. The data were sampled
766 at 10 kHz and filtered at 2 kHz.

767 For optogenetic studies, stimulation of neurons was achieved using a multi-LED array system
768 (CoolLED) connected to the aforementioned Olympus BX51 microscope.

769 **Behavior paradigms**

770 All mice were handled and habituated on the behavioral chamber for 4-5 days before experiments.
771 For optogenetic experiments, mice were tethered to the optic-fiber patch cords and habituated to
772 the context for 15 min daily. For calcium imaging experiments, dummy mini-scope and cable
773 (Inscopix) were fixed on the head of mice and habituated to the context for 20-30 min daily. The
774 behavior arenas were housed inside a soundproof chamber equipment with houselights and video
775 cameras (c920 webcam, Logitech)

776 **Free feeding**

777 Food restricted mice were placed in an empty home cage (20 cm x 32.5cm) with a plastic food
778 container fixed to one corner. Food was freely accessible for 10 min per day during 2 days. For
779 optogenetic experiments, mice were continuously photostimulated for 10min on one day and left
780 with lights off on another day. The light on-off order was pseudo-randomized within a cohort to
781 reduce any effects from the order of photostimulation. After 10 min, the remaining food was
782 weighed. The session was video recorded, and feeding behaviors (e.g., frequency to food
783 container or cumulative time in food container) were also analyzed by EthoVision XT 16.0 video
784 tracking software (Noldus). The recording time for calcium imaging was 15 min.

785 **Social interaction test**

Three-chamber test was performed as previously described [81], but in order to combine with optogenetic and calcium imaging experiments, the door between the chambers was removed. In brief, the novel mice, younger than the test mouse and same gender, were handled for 3 min and then habituated in a wire cage placed in the 3-chamber apparatus for 5–10 min for 4 consecutive days before starting the experiment. The test mouse was located to the center chamber. A wired cup with a novel mouse and an empty cup were introduced into the other two chambers and the sociability test was started. The movement of the test mouse was tracked for 15 min (EthoVision XT 16.0) for calcium imaging. For optogenetic experiments, two days (one day with photostimulation and another day without, but pseudo-randomized order of light on-off epochs within a cohort) were examined and novel mice were changed every day. Sociability was analyzed using cumulative time/frequency in social zone. For each set of experiments, the orientation of the two wired cups containing novel mouse or left empty was counter-balanced.

For several calcium imaging cases, we used a round social arena as described previously [81] or a two-chamber social assay instead of three chambers. In brief, the round-shaped arena (inner diameter: 49 cm, height: 45 cm) was equipped with one 3 d-printed transparent bar cage (diameter: 8cm, height: 10.5 cm) in the center. The inner cage was topped with a cone-shaped 3d-printed roof to prevent the test mouse from climbing up. Inside the cone-shaped roof, a wide-angle (180°) fish-eye lens camera was installed to provide a close-up view of animals' social interactions. Above the arena, a camera at the ceiling was used to track animal's positions and speed. Micro-social behaviors such as exact time point of the start of social interaction or sniffing were measured manually through a wide-angle fish eye camera, as well as automatically tracked by EthoVision XT 16.0 from ceiling camera.

Contextual fear conditioning (cFC)

Main cFC paradigm was modified from a previous study [3]. On day 1, mice were placed into a contextual fear conditioning chamber (Med Associates) while bilaterally connected to optic fiber cables and received three foot-shocks (0.75 mA for 2 sec) at the 198-s, 278-s and 358-s time points. For optogenetic activation experiments, simultaneously with the footshocks, a 10-s, 20-Hz train of 15-ms pulses of 473-nm (10–15 mW) light was used for photostimulation, and constant light of 620 nm (10 mW) was used for photoinhibition. On day 2, mice were connected to optic fiber patch cables and placed in the fear conditioning chamber for 180 s, and neither footshock nor laser light was delivered. Freezing behavior, defined as complete immobility with the exception of breathing, was used as a proxy of fear response. Freezing was automatically quantified using the software ANYmaze 7.2 (Stoelting) as described previously [82] . In brief, the software calculated a “freezing score” depending on the number of pixel changes between frames. If the freezing score fell below an empirically determined threshold for at least 2 s, mice were considered to be freezing. To exclude errors where resting was incorrectly detected as freezing behavior, manually freezing behaviors were verified. Animals were excluded from further analysis if they did not show any freezing behavior upon fear conditioning in a recall session.

Optogenetic manipulations

Mice were bilaterally tied to optic-fiber patch cords (Plexon Inc) connected to a 465-nm LED (for Chr2) via Optogenetic LED module (Plexon Inc) and mating sleeve (Thorlabs). Photostimulation was performed using 10 ms, 463-nm light pulses at 20 Hz and 10 mW. Photoinhibition used constant 620-nm light at 10 mW. The LED was triggered, and pulses were controlled PlexBright 4 Channel Optogenetic Controller by with Radiant Software (Plexon Inc).

Optogenetic conditional place preference (avoidance) test.

Conditioned place preference (CPP) was carried out essentially as previously described[53]. It was conducted in a custom-built arena made of two chambers: a rectangular-shaped 2 chambers (45 * 15 cm); one compartment consisted of white walls and a metal floor with circular holes, the another had red walls and square holes. For the optogenetic experiments, on pretest day (day 1) optic cable tethered mice were freely exploring the chambers without light for 10 min after 5 min of habituation. Based on total time in each chamber, the preferred chamber was identified on that day. For optogenetic activation by Chr2, preference was measured for Lypd1-Cre, but avoidance was measure for Etv1-Cre and Rspo2-Cre mice. Therefore, the preferred chamber was paired with photoactivation for Rspo2-Cre and Etv1-Cre mice, but the non-preferred chamber was paired with photoactivation for Lypd1-Cre mice, for three consecutive conditioning days (day 2-4). During conditioning days mice were constrained in a paired chamber with light for 15 min and another chamber without light for 15 min. On post-test day (day 5) mice were freely exploring the chambers without light the same as on pre-test (day 1). The times each animal spent in each chamber and its locomotor activity (distance travelled) were recorded using EthoVision XT 16.0 (Noldus) tracking software. The preference index was calculated by (duration in the paired chamber) − (duration in the non-paired chamber).

Open field task (OFT)

OFT was carried out essentially as previously described [45]. In brief, four 3-min epochs beginning with a light-off (OFF) baseline epoch, followed by a light-on (ON) illumination epoch, in total a single 12-min session. For analysis, the first light-off and last light-on epochs were excluded in order to avoid novelty or satiation-driven factors.

In vivo Ca^{2+} imaging of freely moving mice

Ca^{2+} videos were acquired at 15 frames per second with an automatic exposure length. An optimal LED power was selected for each mouse to optimize the dynamic range of pixel values in the field of view, and the same LED settings were used for each mouse throughout the series of imaging sessions. Ca^{2+} videos were recorded using nVista acquisition software (Inscopix, Palo Alto, CA). To later account for any lag between the onset of behavior and Ca^{2+} movies, a continuous train of TTL pulses was sent from Ethovision XT 16.0 or ANY-maze 7.1 (Stoelting) to nVista acquisition software at 1 Hz and a 50% duty cycle for the duration of the session to synchronize the extracted behavior statistics with calcium traces. The TTL emission-reception delay is negligible (less than 30ms), therefore the behavioral statistics time series can be synchronized with calcium traces by the emission/receival time on both devices, using a custom python script. We used the IDPS (Inscopix data processing software, version 1.8.0) for the acquisition of calcium image data, rigid motion correction, automatic selection of neuro somata as the regions of interests (ROIs), and extraction of raw calcium traces by using option, Cnmfe in IDPS and visual inspection with their tracing and morphology. To prevent potential biases resulting from temporal convolution in the calcium traces, we performed spike deconvolution using the OASIS algorithm implemented in Suite2p [83]. The inferred spike trains were used in the following social and food preference experiment analyses.

Calcium data analysis for feeding and social interaction assays

The relative distance between the recorded mice and food or other mice are closely related with food consumption and social behavior, respectively. Therefore, we computed this relative distance for each calcium frame recorded in the food consumption or social behavior experiments. This relative distance was then normalized by the radius of the experiment chamber size.

To inspect the correlation between neuron firing rate and the relative distance to food or other animals, we divided the relative distances into 31 bins, and computed the averaged spike firing

rate of the frames whose relative distances fell into the same distance bin. The preferred relative distance of each neuron was determined as the distance bin with the highest averaged firing rate. The neurons were classified into difference valence-correlated categories based on their preferred distance to food / other animals.

Permutation test

In order to confirm that neuronal activities related to specific contexts (food and social assay) beyond chance level (null hypothesis), we rotary shuffled the inferred spike train for each neuron with a random time offset for 1000 times. For each shuffled spike train, we computed the null distance distribution by calculating the averaged firing rate for each distance bin. We used Benjamini–Hochberg procedure[84] to control for a false discovery rate at 5%. Therefore, if the maximum average firing rate of the distance distribution of a neuron was higher than 95% of the null distribution, the neuron was considered significantly tuned to distance to food/social object (Figure 4M-N, Figure 5G-H). To determine if the differences of the percentage of pro/anti food/social neurons between Lypd1, Etv1 and Rspo2 neuron population were significant, we pooled the neurons from the three populations. For each neural population, we randomly selected N neurons from the pool distribution and computed the percentage of pro/anti food/social neurons for 1000 times to obtain a null percentage distribution (N equals the number of neurons for the testing neural population). We then compared the percentage of the testing population with the two tails of the null percentage distribution and determined the significance at the 2.5% significance level (Figure 4O and 5I).

Fear conditioning calcium data analysis

The freezing behaviors are detected automatically by ANY-maze 7.1 (Stoelting) with the 2-second minimum duration. To determine the correlation between neural activities and foot shock/freezing behavior in the fear conditioning experiment, we computed the score for foot shock as follows:

$$Foot\ shock\ response\ score = (F_{during\ shock\ on} - F_{off\ before\ shock})/(F_{during\ shock\ on} + F_{off\ before\ shock})$$

Similarly, the freezing score was computed as:

$$Freezing\ score = (F_{freezing} - F_{non-freezing})/(F_{freezing} + F_{non-freezing})$$

$F_{shock\ on}$ and $F_{freezing}$ are the averaged firing rates in the 2 seconds before and during the onset of foot shock or freezing events, respectively.

The neurons positively correlated with foot shock events might be involved in the negative valence event representation. To investigate this, we computed the percentage of foot-shock correlated neurons in the fear-acquisition session and the freezing frequency in the fear retrieval session for each mouse. We only included mice having neuronal data in both Day 1 and 2. We performed the linear regression on these two statistics for quantitative descriptions of the relationships between these two statistics.

Classification of footshock responsive neurons

In order to classify positive footshock responsive neurons (pro-footshock) or negative footshock responsive neurons (anti-footshock), we rotary shuffled the inferred spike train for each neuron with a random time offset for 1000 times. Then we computed the mean response score to fear stimulus for each shuffled spike train in the same way as described above, in order to obtain a null response score distribution. The neuron whose mean response score was higher than the top 2.5% of the null distribution was considered a pro-footshock neuron whose activity was

positively correlated with a footshock event. Vice versa, a neuron with a response score lower than the bottom 2.5% of the null distribution was considered an anti-footshock neuron.

Immunohistochemistry

For recovery of neurobiotin-filled neurons after whole-cell recordings, acute brain slices were fixed in 4% PFA at room temperature for 30–45 min. Fixed slices were kept in 0.1 M PB (80 mM Na2HPO4 and 20 mM NaH2PO4) until being processed for immunohistochemistry. Slices were then washed in 0.1 M PB and incubated with fluorophore-conjugated streptavidin (1:2,000) (Jackson) diluted in 0.05 M TBS with 0.5% Triton X-100 overnight. The next day, slices were washed in 0.1 M PB and mounted with RapiClear (SunJin Lab Co). Slices were imaged 1 d later.

Histology

Animals were anesthetized IP with a mix of ketamine/xylazine (100 mg/kg and 16 mg/kg, respectively) (Medistar and Serumwerk) and transcardially perfused with ice-cold phosphate-buffered saline (PBS), followed by 4 % PFA (1004005, Merck) (w/v) in PBS. Brains were postfixed at 4 °C in 4 % PFA (w/v) in PBS overnight, embedded in 4 % agarose (#01280, Biomol) (w/v) in PBS, and sliced (50-100 µm) using a Vibratome (VT1000S – Leica). Epifluorescence images were obtained with an upright epifluorescence microscope (Zeiss) with 10x or 5x/0.3 objectives (Zeiss). To acquire Fluorescence z-stack images, a Leica SP8 confocal microscope equipped with a 20x/0.75 IMM objective (Leica) was used. For full views of the brain slices, a tile scan and automated mosaic merge functions of Leica LAS AF software were used. Images were minimally processed with ImageJ software (NIH) to adjust for brightness and contrast for optimal representation of the data, always keeping the same levels of modifications between control and treated animals.

Data Analysis

Data and statistical analyses were performed using Prism v5 (GraphPad, USA) and Excel 2016 (Microsoft, USA). Clampfit software (Molecular Devices, USA) was used to analyze electrophysiological recordings and all statistics are indicated in the figure legends. T-tests or Ordinary one-way ANOVA with Tukey's multiple comparisons test or two-way ANOVA with Bonferroni post-hoc tests were used for individual comparisons of normally distributed data. Normality was assessed using D'Agostino & Pearson normality test. When normality was not assumed Kolmogorov-Smirnov test and Wilcoxon signed-rank test were performed for individual comparisons. P-values represent *p < 0.05; **p < 0.01; ***p < 0.001. All data were represented as the mean ± SEM or STD. All sample sizes and definitions are provided in the figure legends. After the conclusion of experiments, virus-expression and implants placement were verified. Mice with very low or null virus expression were excluded from analysis.

Data availability

Raw and processed snRNAseq data are available at GEO (accession number GSE244860). All relevant data and custom-written analysis code are available from the corresponding author upon reasonable request.

Code availability

Custom-written code is publicly available in a GitHub repository at https://github.com/limserenahansol/1p_BLA_sync_permutation_social_valence

Reference

1. Janak, P. H. & Tye, K. M. From circuits to behaviour in the amygdala. *Nature* **517**, 284–292 (2015).
2. O'Neill, P.-K., Gore, F. & Salzman, C. D. Basolateral amygdala circuitry in positive and negative valence. *Curr Opin Neurobiol* **49**, 175–183 (2018).
3. Kim, J., Pignatelli, M., Xu, S., Itohara, S. & Tonegawa, S. Antagonistic negative and positive neurons of the basolateral amygdala. *Nat Neurosci* **19**, 1636–1646 (2016).

4. Zhang, X. *et al.* Genetically identified amygdala–striatal circuits for valence-specific behaviors. *Nat Neurosci* **24**, 1586–1600 (2021).

5. Namburi, P. *et al.* A circuit mechanism for differentiating positive and negative associations. *Nature* **520**, 675–678 (2015).

6. Beyeler, A. *et al.* Divergent Routing of Positive and Negative Information from the Amygdala during Memory Retrieval. *Neuron* **90**, 348–361 (2016).

7. Klein, R. & Pasterkamp, R. J. Recent advances in inter-cellular interactions during neural circuit assembly. *Curr Opin Neurobiol* **69**, 25–32 (2021).

8. Zhang, X., Kim, J. & Tonegawa, S. Amygdala Reward Neurons Form and Store Fear Extinction Memory. *Neuron* **105**, 1077-1093.e7 (2020).

9. Krabbe, S. *et al.* Adaptive disinhibitory gating by VIP interneurons permits associative learning. *Nat Neurosci* **22**, 1834–1843 (2019).

10. Gründemann, J. *et al.* Amygdala ensembles encode behavioral states. *Science (1979)* **364**, eaav8736 (2019).

11. Saez, A., Rigotti, M., Ostojic, S., Fusi, S. & Salzman, C. D. Abstract Context Representations in Primate Amygdala and Prefrontal Cortex. *Neuron* **87**, 869–881 (2015).

12. Kyriazi, P., Headley, D. B. & Pare, D. Multi-dimensional Coding by Basolateral Amygdala Neurons. *Neuron* **99**, 1315-1328.e5 (2018).

13. Zeng, H. & Sanes, J. R. Neuronal cell-type classification: challenges, opportunities and the path forward. *Nat Rev Neurosci* **18**, 530–546 (2017).

14. O'Leary, T. P. *et al.* Extensive and spatially variable within-cell-type heterogeneity across the basolateral amygdala. *Elife* **9**, e59003 (2020).

15. Swanson, L. W. & Petrovich, G. D. What is the amygdala? *Trends Neurosci* **21**, 323–331 (1998).

16. McDonald, A. J. Neuronal organization of the lateral and basolateral amygdaloid nuclei in the rat. *Journal of Comparative Neurology* **222**, 589–606 (1984).

17. Hintiryan, H. *et al.* Connectivity characterization of the mouse basolateral amygdalar complex. *Nat Commun* **12**, 2859 (2021).

18. Caroline Blanchard, D. & Blanchard, R. J. *INNATE AND CONDITIONED REACTIONS TO THREAT IN RATS WITH AMYGDALOID LESIONS 1*. *Journal of Comparative and Physiological Psychology* vol. 81 (1972).

19. Nader, K., Majidishad, P., Amorapanth, P. & LeDoux, J. E. Damage to the lateral and central, but not other, amygdaloid nuclei prevents the acquisition of auditory fear conditioning. *Learning and Memory* **8**, 156–163 (2001).

20. Everitt, B. J., Cador, M. & Robbins, T. W. Interactions between the amygdala and ventral striatum in stimulus-reward associations: Studies using a second-order schedule of sexual reinforcement. *Neuroscience* **30**, 63–75 (1989).

21. Gallagher, M., Graham, P. W. & Holland, P. C. The amygdala central nucleus and appetitive Pavlovian conditioning: lesions impair one class of conditioned behavior. *The Journal of Neuroscience* **10**, 1906 (1990).

22. Cador, M., Robbins, T. W. & Everitt, B. J. Involvement of the amygdala in stimulus-reward associations: Interaction with the ventral striatum. *Neuroscience* **30**, 77–86 (1989).

23. Hatfield, T., Han, J.-S., Conley, M., Gallagher, M. & Holland, P. Neurotoxic Lesions of Basolateral, But Not Central, Amygdala Interfere with Pavlovian Second-Order Conditioning and Reinforcer Devaluation Effects. *The Journal of Neuroscience* **16**, 5256 (1996).

24. Málková, L., Gaffan, D. & Murray, E. A. Excitotoxic Lesions of the Amygdala Fail to Produce Impairment in Visual Learning for Auditory Secondary Reinforcement But Interfere with Reinforcer Devaluation Effects in Rhesus Monkeys. *The Journal of Neuroscience* **17**, 6011 (1997).

25. Holland, P. C. & Gallagher, M. Double dissociation of the effects of lesions of basolateral and central amygdala on conditioned stimulus-potentiated feeding and Pavlovian-instrumental transfer. *European Journal of Neuroscience* **17**, 1680–1694 (2003).

26. Corbit, L. H. & Balleine, B. W. Double Dissociation of Basolateral and Central Amygdala Lesions on the General and Outcome-Specific Forms of Pavlovian-Instrumental Transfer. *The Journal of Neuroscience* **25**, 962 (2005).

27. Hiroi, N. & White, N. M. The lateral nucleus of the amygdala mediates expression of the amphetamine-produced conditioned place preference. *The Journal of Neuroscience* **11**, 2107 (1991).

28. Chaudhri, N., Woods, C. A., Sahuque, L. L., Gill, T. M. & Janak, P. H. Unilateral inactivation of the basolateral amygdala attenuates context-induced renewal of Pavlovian-conditioned alcohol-seeking. *European Journal of Neuroscience* **38**, 2751–2761 (2013).

29. Tye, K. M. *et al.* Amygdala circuitry mediating reversible and bidirectional control of anxiety. *Nature* **471**, 358–362 (2011).

30. Allsop, S. A., Vander Weele, C. M., Wichmann, R. & Tye, K. M. Optogenetic insights on the relationship between anxiety-related behaviors and social deficits. *Front Behav Neurosci* **8**, (2014).

31. Daviu, N., Bruchas, M. R., Moghaddam, B., Sandi, C. & Beyeler, A. Neurobiological links between stress and anxiety. *Neurobiol Stress* **11**, 100191 (2019).

32. Tripathi, S. J., Chakraborty, S., Srikumar, B. N., Raju, T. R. & Shankaranarayana Rao, B. S. Basolateral amygdalar inactivation blocks chronic stress-induced lamina-specific reduction in prefrontal cortex volume and associated anxiety-like behavior. *Prog Neuropsychopharmacol Biol Psychiatry* **88**, 194–207 (2019).

33. Courtin, J. *et al.* A neuronal mechanism for motivational control of behavior. *Science (1979)* **375**, eabg7277 (2023).

34. Dieterich, A. *et al.* Activation of Basolateral Amygdala to Nucleus Accumbens Projection Neurons Attenuates Chronic Corticosterone-Induced Behavioral Deficits in Male Mice. *Front Behav Neurosci* **15**, (2021).

35. Choi, J.-S. & Kim, J. J. Amygdala regulates risk of predation in rats foraging in a dynamic fear environment. *Proceedings of the National Academy of Sciences* **107**, 21773–21777 (2010).

36. Liu, J. *et al.* Neural Coding of Appetitive Food Experiences in the Amygdala. *Neurobiol Learn Mem* **155**, 261–275 (2018).

37. Baron-Cohen, S. *et al.* The amygdala theory of autism. *Neurosci Biobehav Rev* **24**, 355–364 (2000).

38. Rosenberger, L. A. *et al.* The Human Basolateral Amygdala Is Indispensable for Social Experiential Learning. *Current Biology* **29**, 3532-3537.e3 (2019).

39. Wei, J. *et al.* Amygdala neural ensemble mediates mouse social investigation behaviors. *Natl Sci Rev* **10**, nwac179 (2023).

40. Folkes, O. M. *et al.* An endocannabinoid-regulated basolateral amygdala–nucleus accumbens circuit modulates sociability. *J Clin Invest* **130**, 1728–1742 (2020).

41. Matthews, G. A. *et al.* Dorsal Raphe Dopamine Neurons Represent the Experience of Social Isolation. *Cell* **164**, 617–631 (2016).

42. Huang, W.-C., Zucca, A., Levy, J. & Page, D. T. Social Behavior Is Modulated by Valence-Encoding mPFC-Amygdala Sub-circuitry. *Cell Rep* **32**, 107899 (2020).

43. Lee, C. R., Chen, A. & Tye, K. M. The neural circuitry of social homeostasis: Consequences of acute versus chronic social isolation. *Cell* **184**, 1500–1516 (2021).

44. Felix-Ortiz, A. C. & Tye, K. M. Amygdala Inputs to the Ventral Hippocampus Bidirectionally Modulate Social Behavior. *The Journal of Neuroscience* **34**, 586 (2014).

45. Felix-Ortiz, A. C. *et al.* BLA to vHPC Inputs Modulate Anxiety-Related Behaviors. *Neuron* **79**, 658–664 (2013).

46. Fustiñana, M. S., Eichlisberger, T., Bouwmeester, T., Bitterman, Y. & Lüthi, A. State-dependent encoding of exploratory behaviour in the amygdala. *Nature* **592**, 267–271 (2021).

47. Bugeon, S. *et al.* A transcriptomic axis predicts state modulation of cortical interneurons. *Nature* **607**, 330–338 (2022).

48. Harris, K. D. *et al.* Classes and continua of hippocampal CA1 inhibitory neurons revealed by single-cell transcriptomics. *PLoS Biol* **16**, e2006387- (2018).

49. Hochgerner, H. *et al.* Cell types in the mouse amygdala and their transcriptional response to fear conditioning. *bioRxiv* 2022.10.25.513733 (2022) doi:10.1101/2022.10.25.513733.

50. Cheong, R. Y., Czieselsky, K., Porteous, R. & Herbison, A. E. Expression of ESR1 in Glutamatergic and GABAergic Neurons Is Essential for Normal Puberty Onset, Estrogen Feedback, and Fertility in Female Mice. *The Journal of Neuroscience* **35**, 14533 (2015).

51. Hintiryan, H. *et al.* Connectivity characterization of the mouse basolateral amygdalar complex. *Nat Commun* **12**, 2859 (2021).

52. Ghosh, K. K. *et al.* Miniaturized integration of a fluorescence microscope. *Nat Methods* **8**, 871–878 (2011).

53. Ponserre, M., Fermani, F., Gaitanos, L. & Klein, R. Encoding of Environmental Cues in Central Amygdala Neurons during Foraging. *Journal of Neuroscience* **42**, 3783–3796 (2022).

54. Yao, Z. *et al.* A high-resolution transcriptomic and spatial atlas of cell types in the whole mouse brain. *bioRxiv* 2023.03.06.531121 (2023) doi:10.1101/2023.03.06.531121.

55. LeDoux, J. E., Cicchetti, P., Xagoraris, A. & Romanski, L. M. The lateral amygdaloid nucleus: sensory interface of the amygdala in fear conditioning. *The Journal of Neuroscience* **10**, 1062 (1990).

56. Beyeler, A. *et al.* Organization of Valence-Encoding and Projection-Defined Neurons in the Basolateral Amygdala. *Cell Rep* **22**, 905–918 (2018).

57. Peters, C. *et al.* Transcriptomics reveals amygdala neuron regulation by fasting and ghrelin thereby promoting feeding. *Sci Adv* **9**, eadf6521 (2023).

58. Uwano, T., Nishijo, H., Ono, T. & Tamura, R. Neuronal responsiveness to various sensory stimuli, and associative learning in the rat amygdala. *Neuroscience* **68**, 339–361 (1995).

59. Mazuski, C. & O'Keefe, J. Representation of ethological events by basolateral amygdala neurons. *Cell Rep* **39**, (2022).

60. Gründemann, J. & Lüthi, A. Ensemble coding in amygdala circuits for associative learning. *Curr Opin Neurobiol* **35**, 200–206 (2015).

61. Kyriazi, P., Headley, D. B. & Paré, D. Different Multidimensional Representations across the Amygdalo-Prefrontal Network during an Approach-Avoidance Task. *Neuron* **107**, 717-730.e5 (2020).

62. Fustiñana, M. S., Eichlisberger, T., Bouwmeester, T., Bitterman, Y. & Lüthi, A. State-dependent encoding of exploratory behaviour in the amygdala. *Nature* **592**, 267–271 (2021).

63. Goosens, K. A. & Maren, S. Contextual and Auditory Fear Conditioning are Mediated by the Lateral, Basal, and Central Amygdaloid Nuclei in Rats. *Learning & Memory* **8**, 148–155 (2001).

64. Gore, F. *et al.* Neural Representations of Unconditioned Stimuli in Basolateral Amygdala Mediate Innate and Learned Responses. *Cell* **162**, 134–145 (2015).

65. Nicolas, C. *et al.* Linking emotional valence and anxiety in a mouse insula-amygdala circuit. *Nat Commun* **14**, 5073 (2023).

66. Huang, W.-C., Zucca, A., Levy, J. & Page, D. T. Social Behavior Is Modulated by Valence-Encoding mPFC-Amygdala Sub-circuitry. *Cell Rep* **32**, 107899 (2020).

67. Soriano, P. Generalized lacZ expression with the ROSA26 Cre reporter strain. *Nat Genet* **21**, 70–71 (1999).

68. Madisen, L. *et al.* A robust and high-throughput Cre reporting and characterization system for the whole mouse brain. *Nat Neurosci* **13**, 133–140 (2010).

69. Saunders, A. *et al.* Molecular Diversity and Specializations among the Cells of the Adult Mouse Brain. *Cell* **174**, 1015-1030.e16 (2018).

70. Matson KJE, S. A. J. K. K. M. K. M. L. A. Isolation of Adult Spinal Cord Nuclei for Massively Parallel Single-nucleus RNA Sequencing. *J Vis Exp* (2018).

71. Mathys, H. *et al.* Single-cell transcriptomic analysis of Alzheimer's disease. *Nature* **570**, 332–337 (2019).

72. Beyeler, A. & Dabrowska, J. Chapter 3 - Neuronal diversity of the amygdala and the bed nucleus of the stria terminalis. in *Handbook of Behavioral Neuroscience* (eds. Urban, J. H. & Rosenkranz, J. A.) vol. 26 63–100 (Elsevier, 2020).

73. Kim, J., Zhang, X., Muralidhar, S., LeBlanc, S. A. & Tonegawa, S. Basolateral to Central Amygdala Neural Circuits for Appetitive Behaviors. *Neuron* **93**, 1464-1479.e5 (2017).

74. Kuerbitz, J. *et al.* Loss of Intercalated Cells (ITCs) in the Mouse Amygdala of Tshz1 Mutants Correlates with Fear, Depression, and Social Interaction Phenotypes. *Journal of Neuroscience* **38**, 1160–1177 (2018).

75. Rataj-Baniowska, M. *et al.* Retinoic Acid Receptor β Controls Development of Striatonigral Projection Neurons through FGF-Dependent and Meis1-Dependent Mechanisms. *The Journal of Neuroscience* **35**, 14467 (2015).

76. O'Leary, T. P. *et al.* Extensive and spatially variable within-cell-type heterogeneity across the basolateral amygdala. *Elife* **9**, e59003 (2020).

77. Wang, Y. *et al.* Multimodal mapping of cell types and projections in the central nucleus of the amygdala. *bioRxiv* 2022.10.19.512845 (2022) doi:10.1101/2022.10.19.512845.

78. Rossi, M. A. *et al.* Transcriptional and functional divergence in lateral hypothalamic glutamate neurons projecting to the lateral habenula and ventral tegmental area. *Neuron* **109**, 3823-3837.e6 (2021).

79. Wang, Y. *et al.* EASI-FISH for thick tissue defines lateral hypothalamus spatio-molecular organization. *Cell* **184**, 6361-6377.e24 (2021).

80. Abs, E. *et al.* Learning-Related Plasticity in Dendrite-Targeting Layer 1 Interneurons. *Neuron* **100**, 684-699.e6 (2018).

81. Kim, S. *et al.* Impaired learning and memory in CD38 null mutant mice. *Mol Brain* **9**, 16 (2016).

82. Klein, A. S., Dolensek, N., Weiand, C. & Gogolla, N. Fear balance is maintained by bodily feedback to the insular cortex in mice. *Science (1979)* **374**, 1010–1015 (2021).

83. Pachitariu, M., Stringer, C. & Harris, K. D. Robustness of Spike Deconvolution for Neuronal Calcium Imaging. *The Journal of Neuroscience* **38**, 7976 (2018).

84. Benjamini, Y. & Hochberg, Y. Controlling the False Discovery Rate: A Practical and Powerful Approach to Multiple Testing. *Journal of the Royal Statistical Society: Series B (Methodological)* **57**, 289–300 (1995).

Acknowledgements

We thank Pilar Alcalá for her support in snRNA seq preparation, Yuhan Wang (Janelia Research Campus) for her input in smFISH analysis, Jan Gründemann (DZNE) and Christian Mayer (MPIBI) for their scientific advice during the entire project, Mark Hübener (MPIBI) for reviewing the manuscript. This study was supported by the Max-Planck Society and the European Research Council under the European Union's Horizon 2020 research and innovation programme (no. 885192, BrainRedesign).

Author contributions

HL and RK conceptualized and designed the study. HL conducted and analyzed most experiments and data. YZ supported constructing calcium-imaging analysis pipeline. CP performed electrophysiology experiments. JM supported preparation of smFISH and behavioral experiments. TS contributed to snRNAseq data analysis. HL and RK wrote the paper with input from all authors. RK supervised and provided funding.

Competing interests

The authors declare no competing interests.

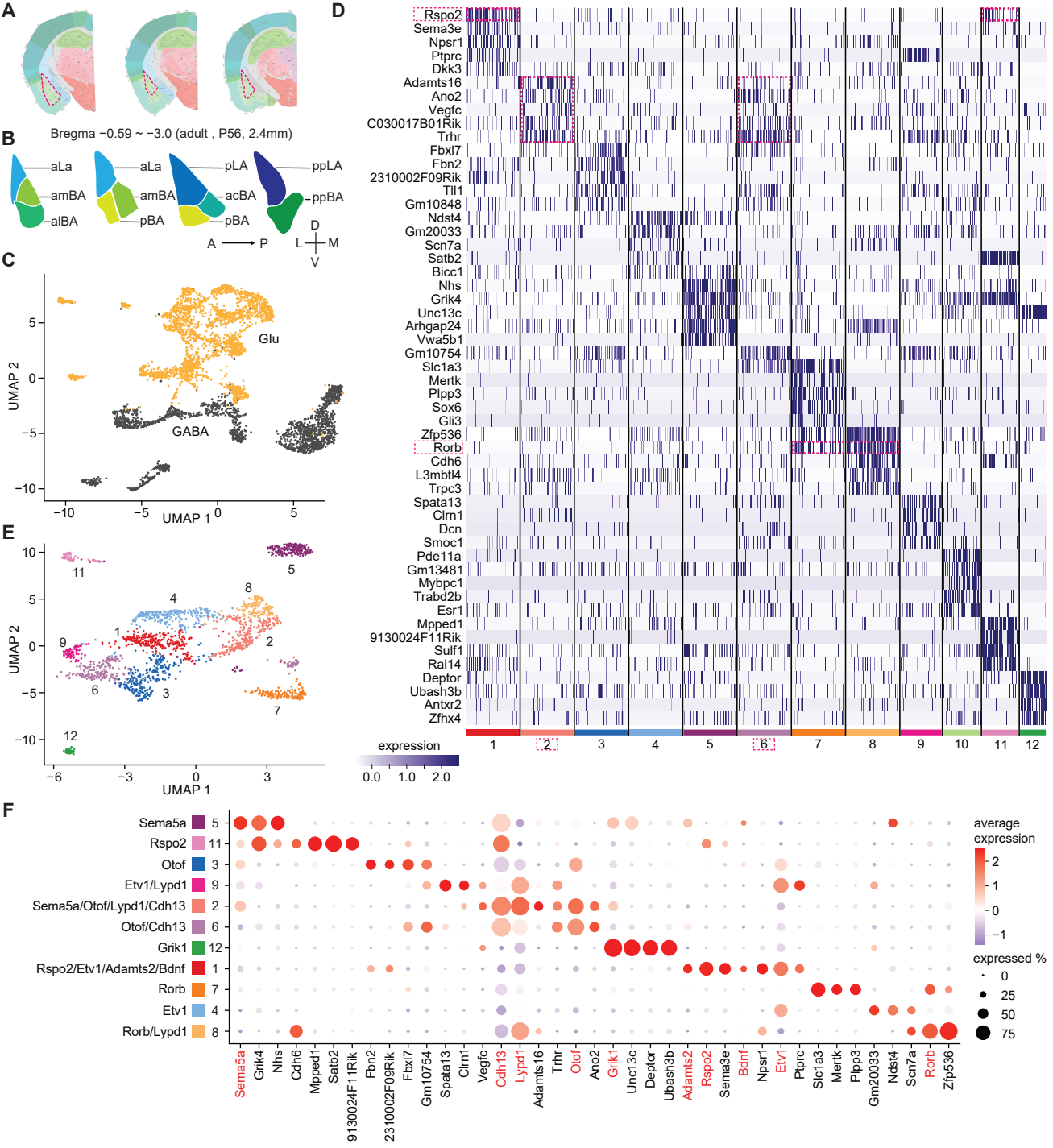
A
B
Bregma −0.59 ~ −3.0 (adult , P56, 2.4mm)
aLa
amBA
alBA
pBA
pLA
acBA
ppLA
ppBA
A
P
D
L
M
V
C
UMAP 2
UMAP 1
Glu
GABA
E
D
Rspo2
Sema3e
Npsr1
Ptprc
Dkk3
Adamts16
Ano2
Vegfc
C030017B01Rik
Trhr
Fbxl7
Fbn2
2310002F09Rik
Tll1
Gm10848
Ndst4
Gm20033
Scn7a
Satb2
Bicc1
Nhs
Grik4
Unc13c
Arhgap24
Vwa5b1
Gm10754
Slc1a3
Mertk
Plpp3
Sox6
Gli3
Zfp536
Rorb
Cdh6
L3mbtl4
Trpc3
Spata13
Clrn1
Dcn
Smoc1
Pde11a
Gm13481
Mybpc1
Trabd2b
Esr1
Mpped1
9130024F11Rik
Sulf1
Rai14
Deptor
Ubash3b
Antxr2
Zfhx4
1 2 3 4 5 6 7 8 9 10 11 12
expression
0.0 1.0 2.0
F
Sema5a 5
Rspo2 11
Otof 3
Etv1/Lypd1 9
Sema5a/Otof/Lypd1/Cdh13 2
Otof/Cdh13 6
Grik1 12
Rspo2/Etv1/Adamts2/Bdnf 1
Rorb 7
Etv1 4
Rorb/Lypd1 8
Sema5a Grik4 Nhs Cdh6 Mpped1 Satb2 9130024F11Rik Fbn2 2310002F09Rik Fbxl7 Gm10754 Spata13 Clrn1 Vegfc Cdh13 Lypd1 Adamts16 Trhr Otof Ano2 Grik1 Unc13c Deptor Ubash3b Adamts2 Rspo2 Sema3e Bdnf Npsr1 Etv1 Ptprc Slc1a3 Mertk Plpp3 Gm20033 Ndst4 Scn7a Rorb Zfp536
average expression
2 1 0 −1
expressed %
0 25 50 75

Main figure legends

Figure 1. Single-nuclei transcriptomic characterization of adult BLA neuron types

(A) Schemes showing the sampled BLA regions highlighted with a triangle. The anterior-posterior extent of the samples ranged from bregma 0.59 ~-3.0 covering around 2.4mm.

(B) Schemes showing regional parcellation of the BLA along the anterior-posterior axis (adapted from [17]). Abbreviations: acBA, anterior-caudal BA; aLA, anterior LA; alBA, anterior-lateral BA; amBA, anterior-medial BA; pBA, posterior BA; pLA, posterior LA; ppBA, posterior-posterior BA; ppLA, posterior-posterior LA.

(C) UMAP of BLA neurons (n=4,544) with cells classified as GABAergic (GABA, n=2,033, black) and glutamatergic (Glu, n=2,511, orange), respectively.

(D) Heatmap of the top 5 marker genes in each cluster of glutamatergic neurons.

(E) UMAP of glutamatergic neuron clusters after separate dimension reduction and clustering. Cell type color palette reflects the one shown in panel F.

(F) Molecular signatures of glutamatergic clusters in dot plot visualization of average gene expression of selected candidate genes. Genes highlighted in red were selected as ten key markers; percentage of cells expressing the selected marker is indicated by circle size and average gene expression level by color scale.

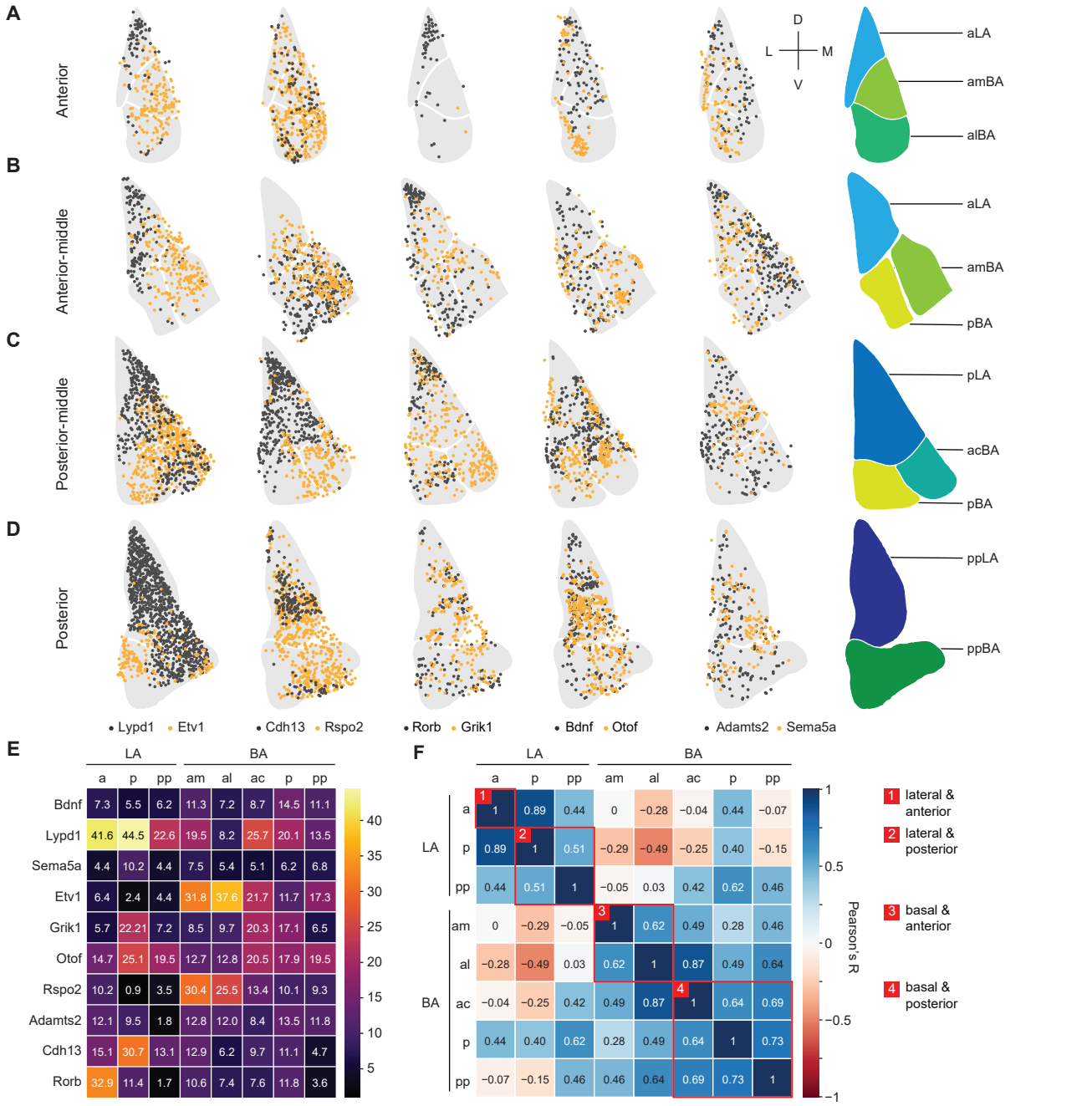
A
Anterior
B
Anterior-middle
C
Posterior-middle
D
Posterior
D
L
M
V
aLA
amBA
alBA
aLA
amBA
pBA
pLA
acBA
pBA
ppLA
ppBA
Lypd1
Etv1
Cdh13
Rspo2
Rorb
Grik1
Bdnf
Otof
Adamts2
Sema5a
E
LA
BA
a p pp am al ac p pp
Bdnf 7.3 5.5 6.2 11.3 7.2 8.7 14.5 11.1
Lypd1 41.6 44.5 22.6 19.5 8.2 25.7 20.1 13.5
Sema5a 4.4 10.2 4.4 7.5 5.4 5.1 6.2 6.8
Etv1 6.4 2.4 4.4 31.8 37.6 21.7 11.7 17.3
Grik1 5.7 22.21 7.2 8.5 9.7 20.3 17.1 6.5
Otof 14.7 25.1 19.5 12.7 12.8 20.5 17.9 19.5
Rspo2 10.2 0.9 3.5 30.4 25.5 13.4 10.1 9.3
Adamts2 12.1 9.5 1.8 12.8 12.0 8.4 13.5 11.8
Cdh13 15.1 30.7 13.1 12.9 6.2 9.7 11.1 4.7
Rorb 32.9 11.4 1.7 10.6 7.4 7.6 11.8 3.6
40
35
30
25
20
15
10
5
F
LA
BA
a p pp am al ac p pp
a 1 0.89 0.44 0 −0.28 −0.04 0.44 −0.07
p 0.89 1 0.51 −0.29 −0.49 −0.25 0.40 −0.15
pp 0.44 0.51 1 −0.05 0.03 0.42 0.62 0.46
am 0 −0.29 −0.05 1 0.62 0.49 0.28 0.46
al −0.28 −0.49 0.03 0.62 1 0.87 0.49 0.64
ac −0.04 −0.25 0.42 0.49 0.87 1 0.64 0.69
p 0.44 0.40 0.62 0.28 0.49 0.64 1 0.73
pp −0.07 −0.15 0.46 0.46 0.64 0.69 0.73 1
1
2
3
4
1
0.5
0
−0.5
−1
Pearson's R
1 lateral & anterior
2 lateral & posterior
3 basal & anterior
4 basal & posterior

Figure 2. Distribution of cells positive for selected marker genes in BLA subregions

(A-D) Distribution of cells within BLA subregions along anterior-posterior axis. Examples of five pairs of marker genes colored in black and yellow are shown from left to right.

(E) Quantification of distribution of cells positive for a specific marker gene within BLA subregions. Heatmap indicating large fractions of cells in yellow and small fractions in dark purple (Average fraction size in percent is indicated in each tile).

(F) Pearson correlation of averages on percentage of cells expressing each gene in eight subregions; colors indicate Pearson's R and categorized red boxes: re-grouping closely correlated subregions to larger category.

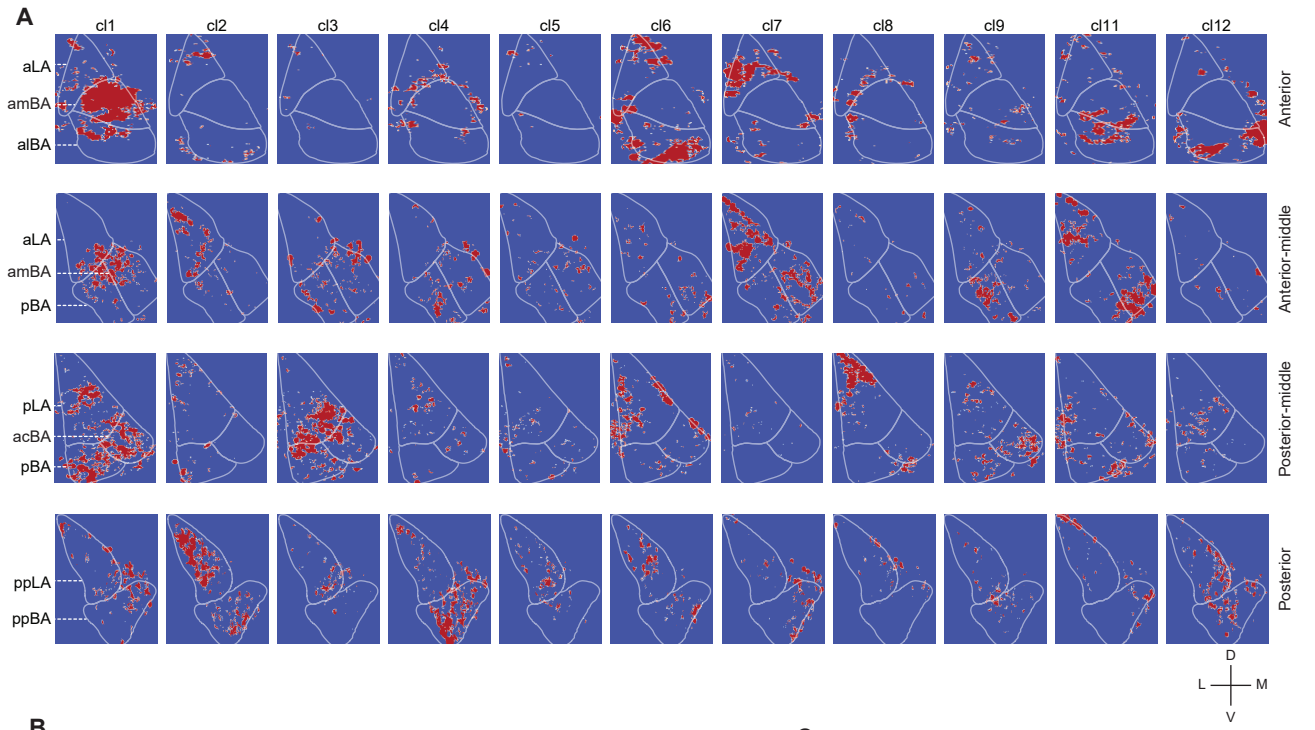
A
cl1
cl2
cl3
cl4
cl5
cl6
cl7
cl8
cl9
cl11
cl12
aLA
amBA
alBA
pBA
pLA
acBA
ppLA
ppBA
Anterior
Anterior-middle
Posterior-middle
Posterior
D
L
M
V

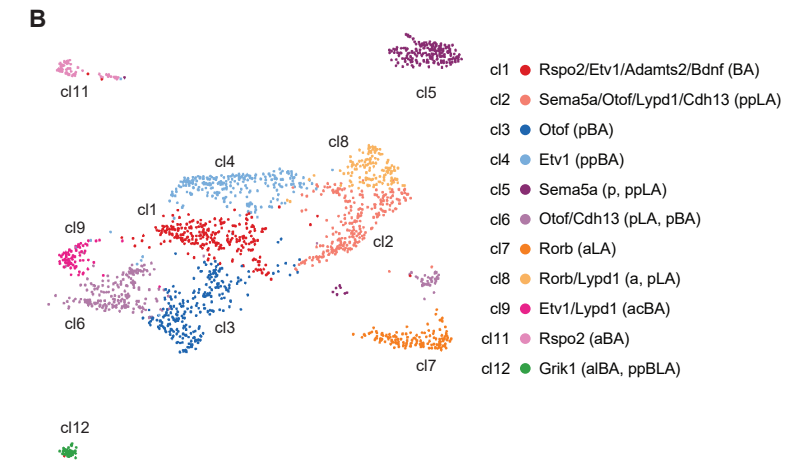
B
cl11
cl5
cl8
cl4
cl1
cl9
cl2
cl6
cl3
cl7
cl12
cl1 Rspo2/Etv1/Adamts2/Bdnf (BA)
cl2 Sema5a/Otof/Lypd1/Cdh13 (ppLA)
cl3 Otof (pBA)
cl4 Etv1 (ppBA)
cl5 Sema5a (p, ppLA)
cl6 Otof/Cdh13 (pLA, pBA)
cl7 Rorb (aLA)
cl8 Rorb/Lypd1 (a, pLA)
cl9 Etv1/Lypd1 (acBA)
cl11 Rspo2 (aBA)
cl12 Grik1 (alBA, ppBLA)

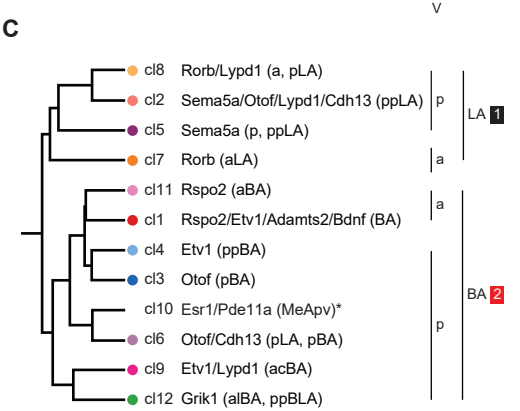
C
cl8 Rorb/Lypd1 (a, pLA)
cl2 Sema5a/Otof/Lypd1/Cdh13 (ppLA)
cl5 Sema5a (p, ppLA)
cl7 Rorb (aLA)
cl11 Rspo2 (aBA)
cl1 Rspo2/Etv1/Adamts2/Bdnf (BA)
cl4 Etv1 (ppBA)
cl3 Otof (pBA)
cl10 Esr1/Pde11a (MeApv)*
cl6 Otof/Cdh13 (pLA, pBA)
cl9 Etv1/Lypd1 (acBA)
cl12 Grik1 (alBA, ppBLA)
p
a
a
p
LA 1
BA 2

Figure 3. Spatial expression of transcriptional clusters

(A) Mapping of snRNA-Seq clusters (11 clusters) to smFISH signals and corresponding locations in the BLA; Panels from top to bottom indicate anterior to posterior sections and colors represent binary expression (Red= expression, Blue = no expression, each cell ID is created after normalization within a radius of 50 μm)

(B) Final annotation of snRNA clusters with respect to expression of markers genes and their distribution in BLA subregions.

(C) Dendrogram of snRNA clusters based on hierarchical clustering of aggregated mRNA expression (Subregions were categorized into large two categories either LA or BA (a, anterior and p, posterior))

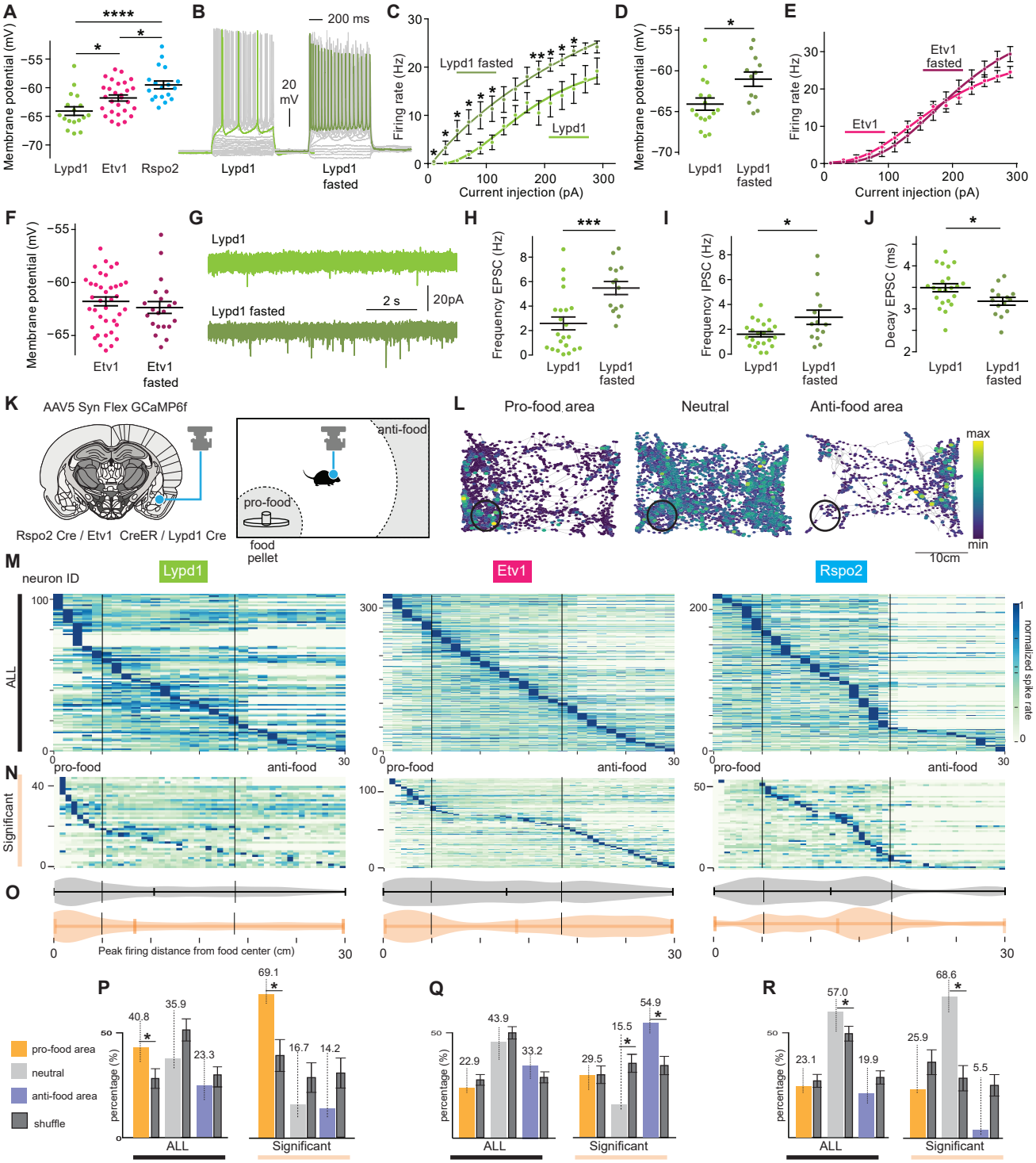
A
Membrane potential (mV)
Lypd1
Etv1
Rspo2
B
200 ms
20 mV
Lypd1
Lypd1 fasted
C
Firing rate (Hz)
Lypd1 fasted
Lypd1
Current injection (pA)
D
Membrane potential (mV)
Lypd1
Lypd1 fasted
E
Firing rate (Hz)
Etv1
Etv1 fasted
Current injection (pA)
F
Membrane potential (mV)
Etv1
Etv1 fasted
G
Lypd1
Lypd1 fasted
2 s
20pA
H
Frequency EPSC (Hz)
Lypd1
Lypd1 fasted
I
Frequency IPSC (Hz)
Lypd1
Lypd1 fasted
J
Decay EPSC (ms)
Lypd1
Lypd1 fasted
K
AAV5 Syn Flex GCaMP6f
Rspo2 Cre / Etv1 CreER / Lypd1 Cre
anti-food
pro-food
food pellet
L
Pro-food area
Neutral
Anti-food area
max
min
10cm
M
neuron ID
Lypd1
Etv1
Rspo2
ALL
pro-food
anti-food
normalized spike rate
N
Significant
pro-food
anti-food
O
Peak firing distance from food center (cm)
P
pro-food area
neutral
anti-food area
shuffle
percentage (%)
40.8
35.9
23.3
69.1
16.7
14.2
ALL
Significant
Q
percentage (%)
22.9
43.9
33.2
29.5
15.5
54.9
ALL
Significant
R
percentage (%)
23.1
57.0
19.9
25.9
68.6
5.5
ALL
Significant

Figure 4. Genetically- and spatially-defined neurons show different feeding-related activities *in vivo and in vitro*

(A) Membrane potentials of three BLA subpopulations (One-way ANOVA, Bonferroni corrected, *p<0.05, ****p<0.0001)
(n=2 mice per group and cell number: Lypd1 = 17, Etv1 = 28 and Rspo2 = 18)

(B) Representative whole-cell current-clamp recordings of BLA^{Lypd1} neurons from fed and fasted animals.

(C, E) Firing rates (Hz) after injecting different current steps in BLA^{Lypd1} neurons (C) and BLA^{Etv1} neurons (E) of fed and fasted animals. (Two-way ANOVA Mixed-effects analysis: Fed vs Fasted, *p<0.05, **p<0.01 for Lypd1, marked in corresponding steps). Lypd1 fed group: n = 17 cells, Lypd1 fasted group: n = 12 cells, Etv1 fed group = 38 cells, Etv1 fasted group: n = 21cells.

(D, F) Membrane potentials in Lypd1 neurons (D) and Etv1 neurons (F) of fed and fasted animals. Unpaired t-test, *p<0.05(Lypd1). Lypd1 fed group: n = 17 cells, Lypd1 fasted group: n = 12 cells, Etv1 fed group = 38 cells, Etv1 fasted group: n = 21cells.

(G) Representative sEPSC recordings in Lypd1 neurons of fed and fasted animals

(H-J) Quantification of sEPSC frequency (H), Decay (J) and sIPSC frequency (I) in Lypd1 neurons of fed and fasted animals. Unpaired t-test, *p<0.05, **p<0.001, ****p<0.0001. Lypd1 fed group: n = 22 cells, Lypd1 fasted group: n = 14 cells.

(K) Schematic explanation of targeted GRIN lens position above GCaMP6f-expressing BLA neurons and free-feeding assay: regions of pro-food and anti-food areas are indicated.

(L) Response map of 3 example neurons whose activities are positively (labelled as pro-food area), negatively (anti-food area) or not correlated (neutral) with the distance to the food chamber, indicated by the black circle. The gray lines indicated the mouse moving trajectories in the chamber. The size and the color of the dots indicate the firing rate of the selected neurons normalized by the maximum firing rate into the range of 0 and 1.

(M, N) Averaged firing rate heatmaps to food distance during the feeding assay in all neurons (M) and in 'significant' neurons whose activity is significantly correlated with the distance to food determined with a permutation test (N). Each row corresponds to a neuron and each column represents a 1 cm distance bin. The pixel values represent the averaged firing rate of the corresponding neurons at the given distance to food normalized by the peak average firing rate

of each neuron. Vertical lines indicate the distance criteria for determining pro-food and anti-food areas. N = 103, 328 and 221 recorded $BLA^{Lypd1,}$ BLA^{Etv1} and BLA^{Rspo2} neurons, respectively.

(O) Violin plots of the peak firing distance of neurons (orange for significant neurons and gray for all neurons). Vertical lines for pro-food and anti-food areas.

(P-R) The percentages of neurons whose firing rates peak in pro-food, neutral and anti-food areas in BLA^{Lypd1} (P), BLA^{Etv1} (Q) and BLA^{Rspo2} (R) populations. Percentage values are indicated in the top of each bar-graph. The significance at the 2.5% significance level in the comparison with the two tails of the null percentage distribution (shuffled) is indicated with an asterisk; shuffled data is shown with SD. The pools of either all neurons or significant neurons are indicated at the bottom of each bar graph.

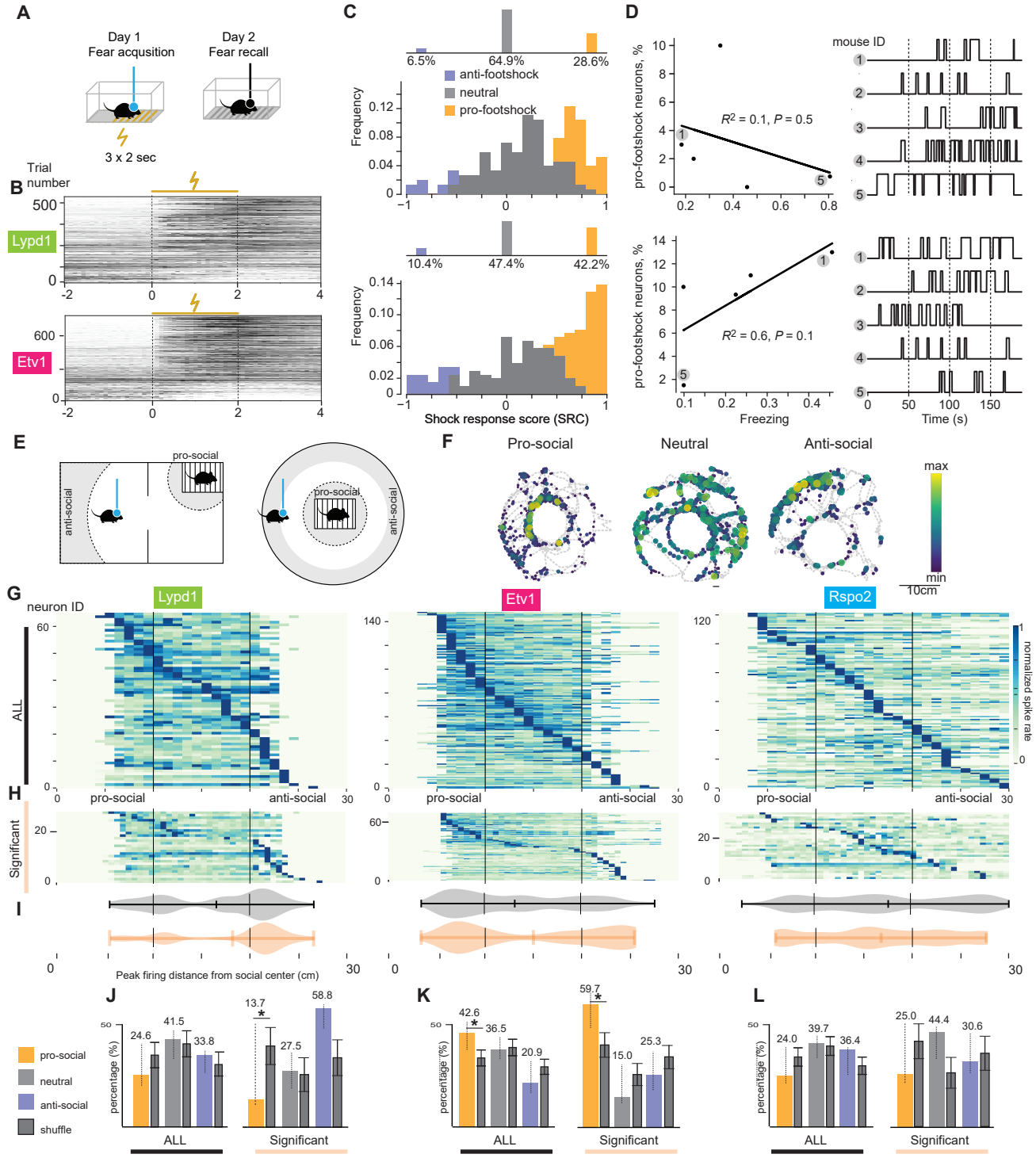
A
Day 1
Fear acqusition
Day 2
Fear recall
3 x 2 sec
B
Trial number
Lypd1
Etv1
C
6.5%
64.9%
28.6%
anti-footshock
neutral
pro-footshock
Frequency
10.4%
47.4%
42.2%
Shock response score (SRC)
D
pro-footshock neurons, %
R^2 = 0.1, P = 0.5
R^2 = 0.6, P = 0.1
Freezing
mouse ID
Time (s)
E
pro-social
anti-social
F
Pro-social
Neutral
Anti-social
max
min
10cm
G
neuron ID
Lypd1
Etv1
Rspo2
ALL
normalized spike rate
pro-social
anti-social
H
Significant
I
Peak firing distance from social center (cm)
J
K
L
percentage (%)
ALL
Significant
pro-social
neutral
anti-social
shuffle

Figure 5. Genetically- and spatially-defined neurons show different responses to aversive and social cues.

(A) Scheme of contextual fear conditioning assay (CFC).

(B) Peri-stimulus time histogram (PSTH) illustrating the inferred spike trains from the calcium responses of the neurons recorded during the footshock session of CFC in Lypd1 (top) and Etv1 (bottom) mice. The vertical dashed line denotes the onset of foot shock stimulus lasting 2s indicated with a yellow line. The footshock trials were sorted by their footshock response score (see method for details) from top to bottom.

(C) Histogram of footshock response score (SRC) of neurons in the BLA ^{Lypd1} (top) and BLA ^{Etv1} (bottom) mice. The neurons whose activities are significantly correlated with footshock events were detected with a permutation test. Within these neurons, the ones with negative correlation ("anti-footshock" neurons) and positive correlation ("pro-footshock") were colored in purple and orange respectively. The neurons which showed no significant correlation ("neutral") were colored in gray. The percentages of pro/anti-footshock and neutral neurons are shown in the bar graph above the histograms.

(D) Scatter plots on the left show the relationship between the freezing frequency in the fear retrieval session (X axis) and the percentages of pro-footshock neurons (Y axis) observed in the fear acquisition session for Etv1 (top) and Lypd1 (bottom) mice (n= 5 mice each). The regression line fitted to the data is represented by the solid line, and the corresponding R2 and p-values are indicated above. The plots on the right show the binarized freezing traces for each mouse (up: freezing, down: no freezing).

(E) Schemes of social interaction assays (two chamber assays with one conspecific in one chamber, or round chamber with conspecific in the center). Pro- and anti-social areas are indicated.

(F) Response maps of 3 example neurons whose activities are positively (labelled as pro-social), negatively (anti-social) or not correlated (neutral) with the distance to the mouse containing cage, indicated by the black circle. The gray lines indicate the mouse moving trajectories in the chamber. The size and the color of the dots indicate the firing rates of the selected neurons normalized by the maximum firing rate into the range of 0 to 1.

(G, H) Averaged firing rate heatmaps to social distance during the social interaction assay in all neurons (G) or in 'significant' neurons whose activity is significantly correlated with the distance

to social chamber determined with a permutation test (H). Each row corresponds to a neuron and each column represents a 1 cm distance bin. Pixel values represent the averaged firing rate of the corresponding neurons at the given distance to social chamber normalized by the peak average firing rate of each neuron. Vertical lines indicate the distance criteria for determining pro-social area and anti-social area. N = 64, 148 and 121 recorded $BLA^{Lypd1,}$ BLA^{Etv1} and BLA^{Rspo2} neurons, respectively.

(I) Violin plots of the peak firing distance of neurons (orange for significant neurons and gray for all neurons). Vertical lines for pro-social and anti-social areas.

(J-L) The percentage of the neurons whose firing rate peak in pro-social, neutral and anti-social area correspondingly in BLA^{Lypd1} (J), BLA^{Etv1} (K) and BLA ^{Rspo2} (L) populations. Percentage values are indicated in the top of each bar-graph. The significance at the 2.5% significance level in the comparison with the two tails of the null percentage distribution (shuffled) is indicated with an asterisk; shuffled data is shown with SD. The pools of either all neurons or significant neurons are indicated at the bottom of each bar graph.

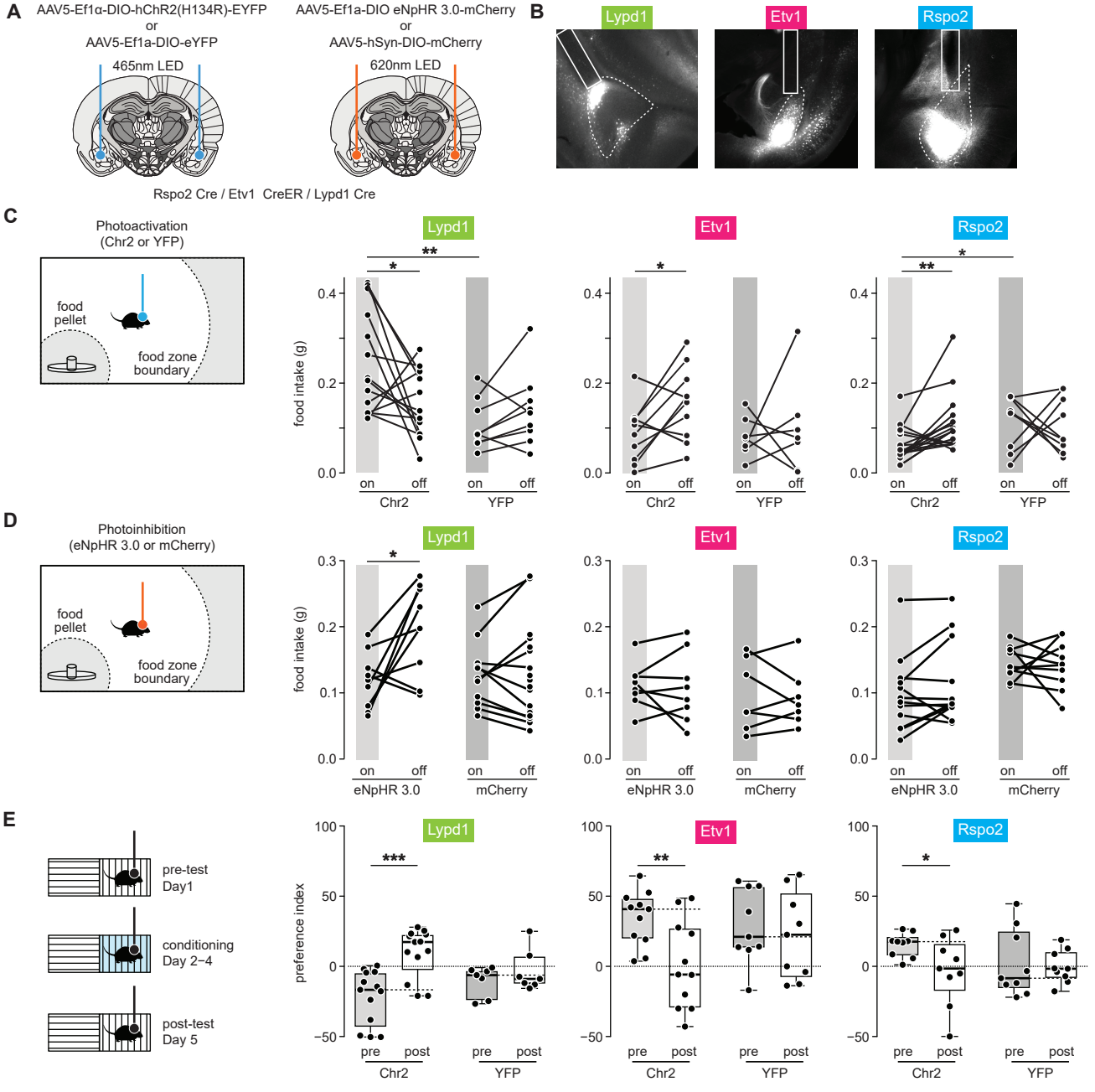
A
AAV5-Ef1α-DIO-hChR2(H134R)-EYFP
or
AAV5-Ef1a-DIO-eYFP
465nm LED
AAV5-Ef1a-DIO eNpHR 3.0-mCherry
or
AAV5-hSyn-DIO-mCherry
620nm LED
B
Lypd1
Etv1
Rspo2
Rspo2 Cre / Etv1 CreER / Lypd1 Cre
C
Photoactivation
(Chr2 or YFP)
food pellet
food zone boundary
food intake (g)
on
off
Chr2
YFP
D
Photoinhibition
(eNpHR 3.0 or mCherry)
eNpHR 3.0
mCherry
E
pre-test
Day1
conditioning
Day 2–4
post-test
Day 5
preference index
pre
post

Figure 6. BLA^{Lypd1} neurons promote normal feeding behavior.

(A) Schemes of AAV injections and optic-fiber placements above ChR2- and eNpHR-expressing BLAs.

(B) Representative images of Chr2-eYFP expression in Rspo2, Etv1 and Lypd1-Cre mice with optic fiber locations.

(C) Left: Scheme of optogenetic activation during the free-feeding assay. Right: Food intake during optogenetic activation of three BLA populations compared to light off epochs and compared to photostimulated control groups. Lypd1 group: n = 14 (ChR2) and 9 mice (YFP) per group with two-tailed paired t test, $t_{(13)}$= 2.457, p= 0.0288 within Chr2 (on versus off) group. For Chr2-On versus YFP-On: two-tailed unpaired t test, t (21) = 3.4, p = 0.0027) *p<0.05, **p<0.01. Etv1 group: n = 8 (Chr2) and 7 mice (YFP) per group with two-tailed paired t test, $t_{(9)}$= 2.492, p= 0.0343 within Chr2 group (on versus off)) *p<0.05. Rspo2 group: n = 18 (Chr2) and 9 mice (YFP) per group with Wilcoxon matched-pairs signed rank test, p=0.0023 within Chr2 (on versus off) group. For Chr2-On versus YFP-On: Kolmogorov-Smirnov test, p = 0.0226, *p<0.05, **p<0.01.

(D) Left: Scheme of optogenetic inhibition during the free-feeding assay. Right: Food intake during optogenetic inhibition of three BLA populations compared to light off epochs and compared to photostimulated control groups. Lypd1 group: n = 9 (eNpHR 3.0) and 11 mice (mCherry) per group with two-tailed paired t test, $t_{(8)}$= 2.771, p= 0.0243 within eNpHR 3.0 (on versus off) group) *p<0.05. Etv1 group: n = 8 (eNpHR 3.0) and 7 mice (mCherry) per group. Rspo2 group: n = 13 (eNpHR 3.0) and 10 mice (mCherry) per group.

(E) Left: Scheme of conditioned-place preference experiment. Right: Preference index (cumulative time % in paired chamber – cumulative time % in unpaired chamber) of cohorts of mice combined with photostimulation of three BLA population before (pre) and after (post) conditioning. In case of Lypd1-Cre mice, the initially non-preferred chamber was paired with light, in case of Etv1-Cre and Rspo2-Cre mice, the initially preferred chamber was paired with light, to observe preference and avoidance, respectively. Lypd1 groups: n = 13 (Chr2) and 7 mice (YFP) per group; two-tailed paired t test, $t_{(12)}$ = 4.528, p = 0.0007 within Chr2 group (pretest versus posttest)), *p<0.05, **p<0.01, ***p<0.001. Etv1 groups: n = 11 (Chr2) and 9 mice (YFP) per group; two-tailed paired t test, $t_{(10)}$ = 3.273, p = 0.0084 within Chr2 group (pretest versus posttest). Rspo2 groups: n = 8 mice (Chr2 and YFP) per group; two-tailed paired t test, $t_{(7)}$ = 2.695, p = 0.0308, within Chr2 group (pretest versus posttest).

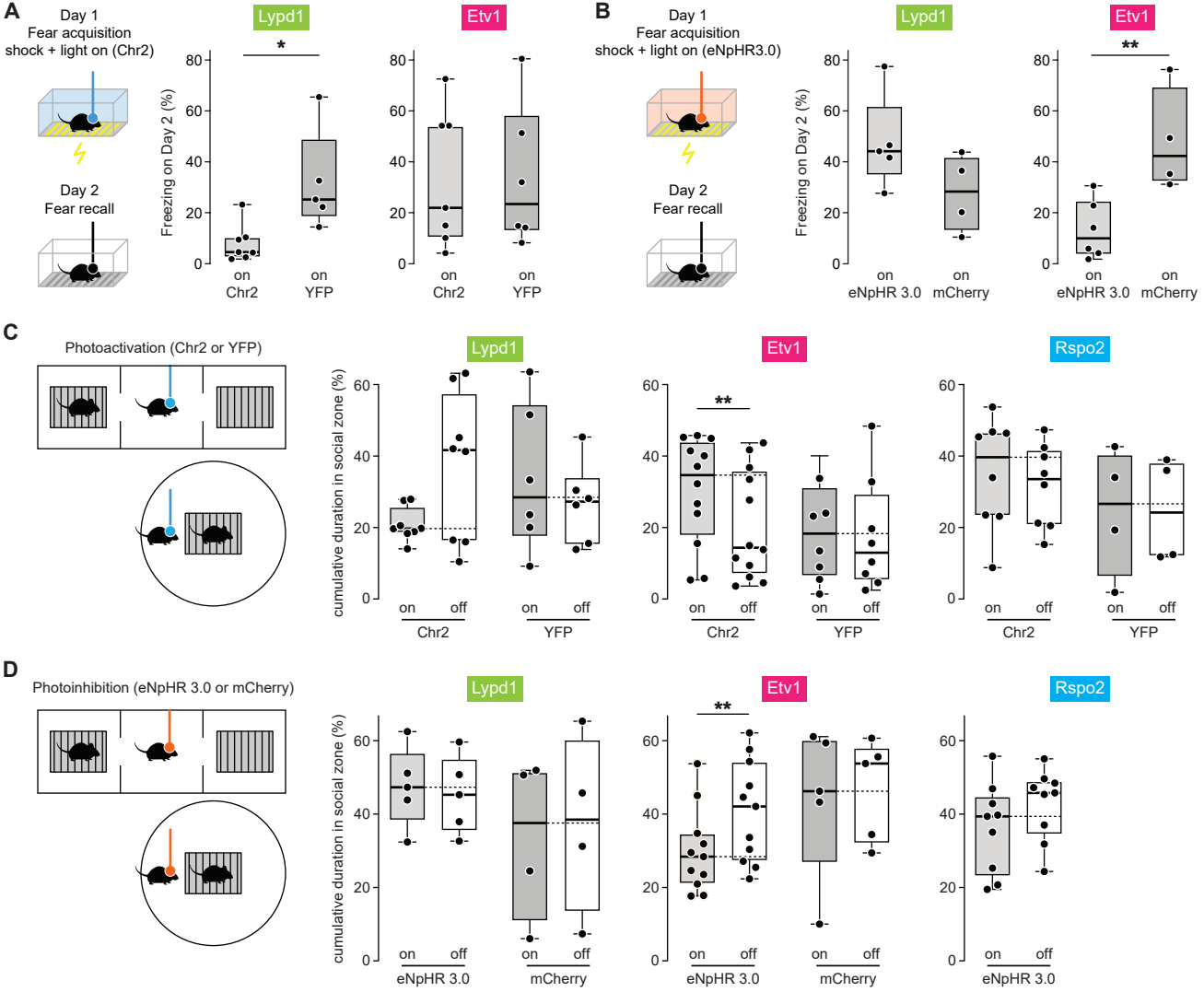
A
Day 1
Fear acquisition
shock + light on (Chr2)
Day 2
Fear recall
Lypd1
Etv1
Freezing on Day 2 (%)
*
on Chr2
on YFP
B
Day 1
Fear acquisition
shock + light on (eNpHR3.0)
Day 2
Fear recall
Lypd1
Etv1
Freezing on Day 2 (%)
**
on eNpHR 3.0
on mCherry
C
Photoactivation (Chr2 or YFP)
Lypd1
Etv1
Rspo2
cumulative duration in social zone (%)
**
on
off
Chr2
YFP
D
Photoinhibition (eNpHR 3.0 or mCherry)
Lypd1
Etv1
Rspo2
cumulative duration in social zone (%)
**
on
off
eNpHR 3.0
mCherry

Figure 7. BLA^{Etv1} neurons are necessary for fear memory formation and social interactions.

(A) Left: Scheme of contextual fear conditioning with photostimulation; day 1 with 3 times of footshocks (0.75mA) paired with light on. Freezing was measured on day 2 (fear recall). Right: Freezing behavior (%) on day 2 combined with photostimulation of two BLA populations in comparison to controls. Lypd1 groups: *n* = 7 (Chr2) and 5 mice (YFP) per group; Kolmogorov-Smirnov test, p = 0.0152, *p<0.05), Etv1 groups: *n* = 6 (Chr2) and 7 (YFP) mice per group; Kolmogorov-Smirnov test, *P* = 0.9254.

(B) Left: Scheme of contextual fear conditioning with photoinhibition; Right: Freezing behavior (%) on day 2 combined with photoinhibition of two BLA populations in comparison to controls. Lypd1 groups: n= 5 (eNpHR 3.0) and 5 (mcherry) mice per group; Kolmogorov-Smirnov test, p = 0.2857. Etv1 groups: n= 6 (eNpHR 3.0) and 4 (mcherry) mice per group; Kolmogorov-Smirnov test, p = 0.0095, **p<0.01.

(C) Schemes of social interaction assays with photoactivation; Right: Cumulative duration in social zone (%) combined with photoactivation of three BLA populations in comparison to light-off epochs and controls. Lypd1 groups; *n* = 8 (Chr2) and 6 mice (YFP) per group; two-tailed paired *t* test, $t_{(7)}$ = 2.307, p = 0.0544 within Chr2 group (on versus off); Etv1 groups; *n* = 12 (Chr2) and 8 mice (YFP) per group; two-tailed paired *t* test, $t_{(11)}$ = 3.785, p = 0.0030 , **p<0.01, within Chr2 group (on versus off); Rspo2 groups; *n* = 6 (Chr2) and 4 mice (YFP) per group; two-tailed paired *t* test, $t_{(7)}$ = 0.6806, p = 0.5180, within Chr2 group (on versus off).

(D) Schemes of social interaction assays with photoinhibition; Right: Cumulative duration in social zone (%) combined with photoinhibition of three BLA populations in comparison to light-off epochs and controls. Lypd1 mice, n= 5 (eNpHR3.0) and 4 mice (mcherry) per group; Wilcoxon matched-pairs signed rank test, p = >0.9999, within eNpHR 3.0 group (on versus off); Etv1 mice, n= 11 (eNpHR3.0) and 5 mice (mcherry) per group; two tailed paired t test, t (10) = 3.19, p = 0.0097, **p<0.01, within eNpHR 3.0 group (on versus off); Rspo2 mice, n= 9 (eNpHR3.0) mice, Wilcoxon matched-pairs signed rank test, p = 0.6250, within eNpHR 3.0 group (on versus off).